## Article

# Local Crystal Misorientation Influences Non-radiative Recombination in Halide Perovskites



Sarthak Jariwala, Hongyu Sun, Gede W.P. Adhyaksa, ..., Bruno Ehrler, Erik C. Garnett, David S. Ginger

dginger@uw.edu

### HIGHLIGHTS

Electron backscatter diffraction (EBSD) reveals grain structure in perovskite films

EBSD maps reveal crystal orientation variations in sub-grain structure

Orientation heterogeneities within grains indicate local strain

Local misorientation spreads within grains influence non-radiative recombination

Understanding the origins of non-radiative recombination centers is critical to improving photovoltaic performance. This study probes structural causes of non-radiative recombination in prototypical halide perovskite semiconductors using electron backscatter diffraction (EBSD). Multimodal microscopy correlating the EBSD with confocal photoluminescence shows that higher local strain leads to higher non-radiative recombination in the studied compositions. Furthermore, larger grains show higher strain. These results help explain why performance in perovskite photovoltaics has not tracked with grain size, pointing the way toward further improvements.

# Joule

**CellPress**

## Article

# Local Crystal Misorientation Influences Non-radiative Recombination in Halide Perovskites

Sarthak Jariwala,[1,2] Hongyu Sun,[3] Gede W.P. Adhyaksa,[3] Andries Lof,[3] Loreta A. Muscarella,[3] Bruno Ehrler,[3] Erik C. Garnett,[3] and David S. Ginger[1,4,*]

## SUMMARY

**We use ultrasensitive electron backscatter diffraction (EBSD) to map the local crystal orientations, grains, and grain boundaries in $CH_3NH_3PbI_3$ (MAPI) perovskite thin films. Although the true grain structure is broadly consistent with the morphology visible in scanning electron microscopy (SEM), the inverse pole figure maps taken with EBSD reveal grain structure and internal misorientation that is otherwise hidden. Local crystal misorientation is consistent with the presence of local strain, which varies from one grain to the next. We acquire co-aligned confocal optical photoluminescence (PL) microscopy images on the same MAPI samples used for EBSD. We correlate optical and EBSD data, showing that PL is anticorrelated with the local grain orientation spread, suggesting that grains with higher degrees of crystalline orientational heterogeneity (local strain) exhibit more non-radiative recombination. We find that larger grains tend to have larger grain orientation spread, consistent with higher degrees of strain and non-radiative recombination.**

## INTRODUCTION

Halide perovskite-based solar cells have experienced rapid gains in power conversion efficiency (PCE), with the current PCE record at 23.7% for single-junction and 28% for Si-perovskite tandems.[1] Despite such high PCE for a material that is solution processed, the values are still well below their realistically achievable PCE limits (~30% for single-junction $CH_3NH_3PbI_3$[2] and ~32% for two-terminal Si-perovskite tandems[3]). Non-radiative recombination, both in the film[4–7] and at the interfaces,[8,9] remains a major barrier to approach the radiative efficiency limits in halide perovskites. Our group has recently demonstrated that with surface passivation, halide perovskites can achieve over 90% internal photoluminescence quantum efficiency (PLQE) and a quasi-Fermi level splitting approaching 97% of the radiative efficiency limit.[4,8] These results put halide perovskites alongside gallium arsenide (GaAs) as one of the most radiatively efficient semiconductors.[10] However, intrinsic films (without surface passivation) have a significant source of non-radiative recombination (with internal PLQE ~10%).[4] A significant portion of this non-radiative recombination is thought to occur at under-passivated surfaces and grain boundaries.[4–6,11–13]

Unfortunately, the casual conflation of grain boundaries with morphological structures in halide perovskites has generated confusion about the nature of grain boundaries.[14,15] This situation has arisen because, currently, one of the most-used techniques to identify grains and grain boundaries in the halide perovskite community is scanning electron microscopy (SEM). However, while SEM provides information

### Context & Scale

Polycrystalline halide perovskite thin films have achieved high photovoltaic power conversion efficiencies but still have room to improve. Grain boundaries are an obvious possible challenge, but the role of grain boundaries has remained confusing: surprisingly, to date there is little correlation between grain size and solar cell efficiency. One challenge has been the prevalent use of non-crystallographic techniques to identify grain size. Using a state-of-the-art electron backscatter diffraction detector, we image the grain and sub-grain structure in perovskites. These measurements indicate the presence of local strain within grains, which further leads to non-radiative recombination and efficiency losses. These findings suggest that growing large grains without significant intragrain strain will enable more efficient devices and indicate that intragrain strain will be useful to characterize when scaling up perovskite thin film deposition for a various optoelectronic device applications.

## Joule

about the morphology of the film, conventional SEM does not provide any crystallographic information about the material. The crystallographic information is critical in the case of halide perovskites because domains as observed in the SEM may not accurately represent the grains and grain boundary terminations, leading to an overestimation of grain sizes.[16] Indeed, frustration with this topic has caused a leading solar cell researcher to tweet out "SEM does not obvious[ly] [provide] information about 'grain size' or 'grain orientation' for metal halide perovskite active layers."[17]

Traditionally, grain sizes, grain boundaries, and local crystal orientations in thin-film materials are mapped using electron backscatter diffraction (EBSD). However, this method has been notoriously difficult to apply to the halide perovskites most relevant for photovoltaics applications due to beam-induced damage.[16,18,19] Compared to SEM imaging, EBSD requires higher doses (higher current and/or longer integration time) to acquire sufficient contrast in the Kikuchi diffraction lines generated from backscattered electrons.[16] Therefore, the use of traditional EBSD detectors leads to significant beam-induced damage when characterizing halide perovskite solar cell materials.[16] Recently, Leonhard et al. reported that using low-vacuum mode with water pressures of 0.1–1 mbar in the sample chamber can minimize beam-induced damage and prevent surface charging due to ionization of the water molecules by the electrons during EBSD.[20] Some of us recently demonstrated the potential for a new solid-state EBSD detector to enable EBSD maps with high sensitivity and fast readout and without appreciable beam damage to the crystal structure.[21]

Understanding grain orientation and grain boundary properties has been critical to the development of many photovoltaic semiconductor technologies such as CdTe, GaAs, $Cu(In_{1-x}Ga_x)Se_2$, multicrystalline Si, and InP.[22–29] However, the role of grain orientation and grain boundary properties in halide perovskite semiconductors has remained poorly understood[30] despite the local optoelectronic heterogeneity observed at the microscale in these materials.[12,13,31,32] Here, we measure the local crystal orientation in solution-processed halide perovskite thin films using EBSD and demonstrate that the SEM morphology is not sufficient to characterize grain structure in these films. More importantly, we investigate the impact of grain-to-grain orientation heterogeneity and sub-grain orientation heterogeneity on local optoelectronic properties. We report the presence of local crystal misorientation leading to local strain within the grains and grain-to-grain orientation spread leading to strain heterogeneity within the film. Furthermore, we use crystallographic identification to unequivocally demonstrate and locate the sub-grain boundaries within individual grains. Lastly, we correlate EBSD and confocal photoluminescence measurements to measure the impact of local grain and sub-grain orientation heterogeneity on local photoluminescence. We observe higher non-radiative recombination in regions with higher orientation heterogeneity and lower non-radiative recombination in regions with lower orientation heterogeneity. Our results provide direct evidence for the impact of local crystal misorientation on the optoelectronic properties in halide perovskite thin films and point the way toward optimization of grain structure for improved photovoltaic performance.

## RESULTS

Using a state-of-the-art solid-state EBSD detector,[21] we optimized the beam current to be 100 pA at 6 kV accelerating voltage with a pixel integration time of 100 ms. We measure the Kikuchi diffraction patterns generated from the backscattered electrons using a traditional EBSD geometry with the electron beam hitting the sample at
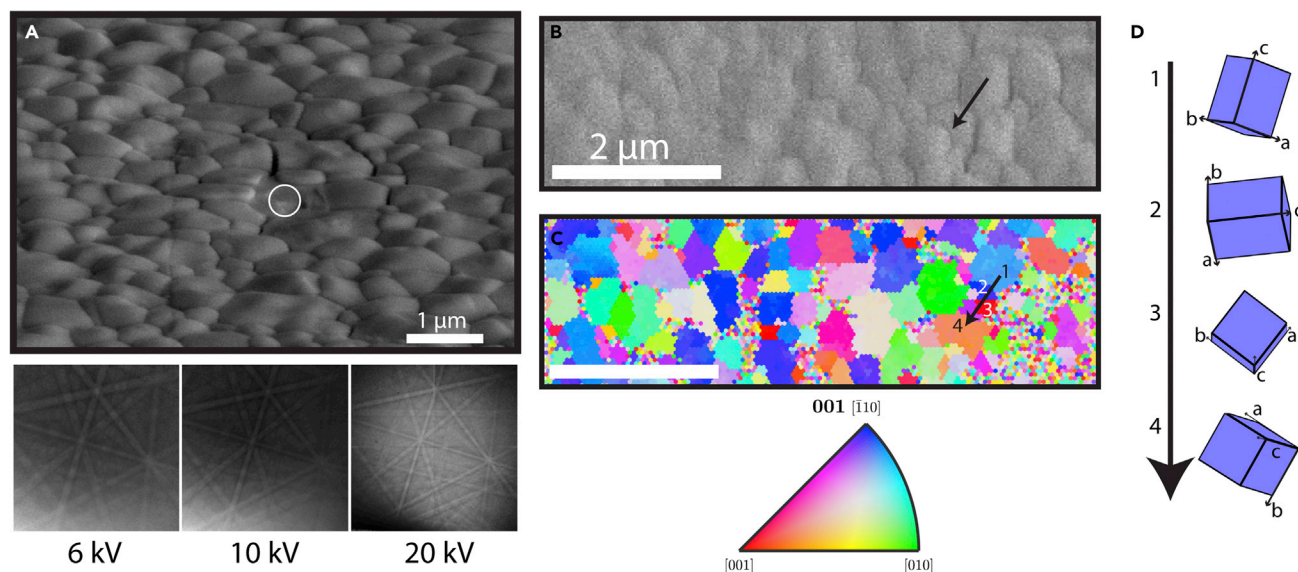
[1]Department of Chemistry, University of Washington, Seattle, WA 98195, USA

[2]Department of Materials Science and Engineering, University of Washington, Seattle, WA 98195, USA

[3]Center for Nanophotonics, AMOLF, 1098 XG, Amsterdam, the Netherlands

[4]Lead Contact

*Correspondence: dginger@uw.edu

https://doi.org/10.1016/j.joule.2019.09.001

# Joule

**CellPress**



**Figure 1. Morphology and Local Crystal Orientation Measurements of CH$_3$NH$_3$PbI$_3$ Thin Films**

(A) Scanning electron microscope (SEM) image of CH$_3$NH$_3$PbI$_3$ thin film tilted at 45° with representative sharp Kikuchi diffraction lines of a measurement point inside a grain (circled) collected in traditional electron backscatter diffraction (EBSD) geometry at 6, 10, and 20 kV accelerating voltage.

(B and C) SEM image (B) and inverse pole figure (IPF) map (C) generated from EBSD of a representative CH$_3$NH$_3$PbI$_3$ film with IPF color key. The 001 (in bold) in the IPF color key indicates that the IPF map plotted is along the sample z direction.

(D) Depiction of changes in local crystal orientation along the black arrow in (B) and (C) as viewed normal to the sample.

See Figure S6 for a higher resolution SEM image of (B) and Figure S4 for another SEM image with IPF map.

70° with respect to the sample surface normal. Kikuchi diffraction lines generated at local Bragg angles contain the information about the local crystal orientation.[33,34] We scan across the sample and collect these Kikuchi patterns at every pixel and generate a local crystal orientation map of CH$_3$NH$_3$PbI$_3$ thin film.

Figure 1A shows an SEM image of a representative CH$_3$NH$_3$PbI$_3$ thin film grown by lead acetate and methylammonium-based precursors with hypophosphorous acid additives (a recipe used for CH$_3$NH$_3$PbI$_3$-based photovoltaics; see Experimental Procedures for details)[35] and corresponding sharp Kikuchi patterns obtained at 6, 10, and 20 kV. Consistent with X-ray diffraction (XRD) (Figure S1), the sharp Kikuchi patterns indicate that these films are crystalline. Moreover, these results demonstrate that we can acquire sharp patterns at the relatively low accelerating voltage of 6 kV (acquired for only 100 ms per pixel), confirming the high sensitivity and fast readout of this new EBSD detector. Figures 1B and 1C show the SEM image of a CH$_3$NH$_3$PbI$_3$ film and the corresponding inverse pole figure (IPF) map generated from fitting the Kikuchi patterns to a tetragonal CH$_3$NH$_3$PbI$_3$ structure[36,37] (see Note S1 for details and Figure S2 for comparison of indexed results to other phases) at every pixel, with an IPF color key. An IPF map shows the projection of the sample coordinate system (xyz) in the crystal coordinate system (abc). We note that the films have strong orientation along the [110] direction along the sample z axis as evident from the pole density figure (Figure S3). Importantly, these data provide direct evidence for the crystallographic parameters and existence of grain boundaries in these CH$_3$NH$_3$PbI$_3$ thin films.

Broadly, we see that the SEM image in Figure 1B and the EBSD image in Figure 1C are in relatively good agreement. Most of the "grains" observed in SEM are indeed also present in the EBSD image (Figures S4 and S5). However, while the features
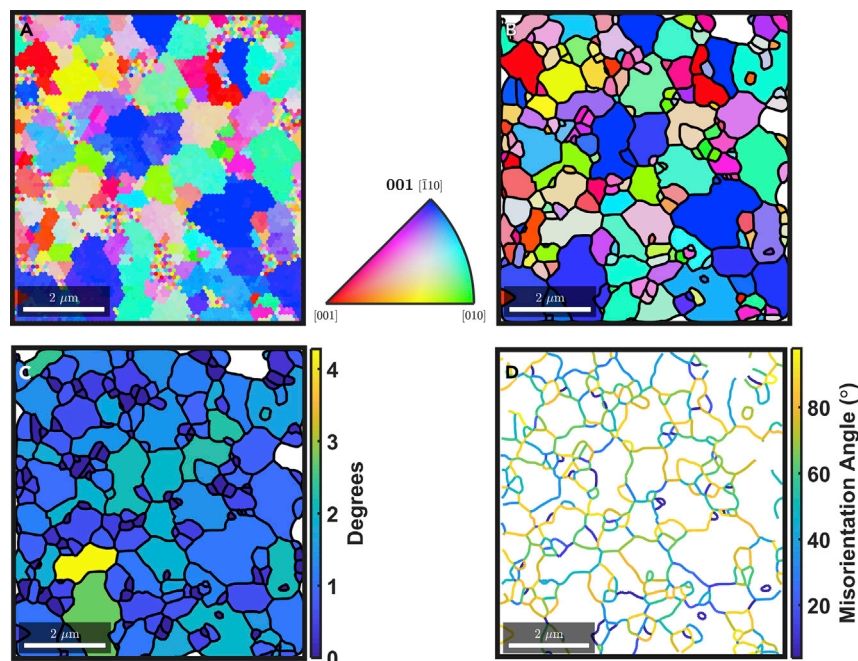
**Figure 2. Imaging the Local Orientation Heterogeneity, Grains, and Grain Boundaries in CH$_3$NH$_3$PbI$_3$ Thin Films Using Electron Back Scatter Diffraction (EBSD)**

(A) Inverse pole figure (IPF) map of CH$_3$NH$_3$PbI$_3$ generated using EBSD and IPF color key.

(B) Grains identified from IPF map with a 4° orientation threshold and plotted with their mean orientation.

(C) Plot of grain orientation spread (GOS) showing grain-to-grain heterogeneity in average local misorientation in the same film.

(D) Grain boundary network with their respective misorientation angles showing the degree of misorientation between two neighboring grains.

(B), (C), and (D) have the same orientation threshold (4°). See Figure S9 for SEM image of the region.

observed in SEM are generally consistent with grain structure obtained from EBSD measurements (Figures S4 and S5), we emphasize that the EBSD maps provide critical information missing from the SEM images. For example, based on SEM morphology alone, the black arrow in the SEM image in Figure 1B would be assigned as going across a single "grain boundary." However, from the corresponding IPF map (Figure 1C) we note that the film actually possesses 3 distinct boundaries separating 4 different local crystal orientation changes along the same arrow. Figure 1D depicts the changes in the local crystal orientation occurring across the arrow shown in Figures 1B and 1C (see Figure S6 for higher resolution SEM image of Figure 1B and along the arrow). These results show that several large "grains" as seen in SEM image are composed of many smaller grains, similar to observations made using transmission electron microscope[38,39] and using EBSD in large grain (~50 μm) CH$_3$NH$_3$PbBr$_3$ samples.[21] Indeed, these differences between SEM and EBSD perhaps provide another reason why efforts to relate morphological grain boundaries with carrier dynamics have not always found clear correlations.[15]

Figure 2A shows the IPF map of another typical CH$_3$NH$_3$PbI$_3$ thin film. By assigning an appropriate threshold for misorientation (4°; see Figure S7 for results from different threshold values), we can assign each pixel in the IPF to a grain, and hence identify the grains and grain boundaries[40] (see Note S1 and Figure S8 for more details on grain detection). Figure 2B shows the crystal grains identified by this approach, along with their grain boundaries. These maps provide a quantifiable

**Joule**

**CellPress**

identification of the grains and their orientation, revealing boundaries not visible in the SEM morphology images (see Figure S9 for SEM image of the region in Figure 2).

In addition to identifying grains and grain boundaries, the analysis of the IPF data in Figure 2 provides an additional level of insight regarding crystallographic misorientation within individual grains. For example, we observe local variations in crystal orientations within individual grains (Figure S10) across the entire film that exceed the orientation noise in local crystallographic orientation obtained from fitting the Kikuchi pattern (see Note S1 for details). Figure 2B plots the grains identified in Figure 2A, color coded according to their mean orientation.[41,42] The average deviation in orientation between each pixel (point) within a grain and the mean grain orientation of that grain is defined as the grain orientation spread (GOS).[43] Figure 2C plots the GOS values in the same region as Figures 2A and 2B of this representative $CH_3NH_3PbI_3$ thin film. Importantly, we observe a range of grain-to-grain orientational heterogeneity in the film with GOS values as low as 0° (perfectly ordered) and as high as 4.3° of orientation spread within individual grains. These grain-to-grain local variations in crystal orientation are indicative of local strain distributions within the grains.[43] Higher GOS values indicate grains with higher strain, and lower GOS values indicate grains with lower strain.[43] We note that the misorientation within the grain and between neighboring points observed is not a consequence of beam-induced degradation in the material (see Figure S11). These results demonstrate the existence of potentially important local structural and strain heterogeneity in halide perovskite thin films stemming from the local crystal orientation variations. These results are consistent with, but provide better resolution than, those of Stranks et al., who recently reported strain heterogeneity at long length scales in halide perovskite thin films based on μ-XRD measurements.[38] Importantly, our results further demonstrate that the local strain heterogeneity observed in halide perovskite semiconductors originates from local crystal misorientation within grains. In most semiconductors, local lattice imperfections, such as local crystal orientation changes within grains observed here, can act as non-radiative recombination centers,[44] which in turn would have a significant influence on the performance of perovskite solar cells. We will explore this possibility in more detail below.

Alongside local crystal orientation heterogeneity, orientation imaging using EBSD also allows us to probe and understand the nature of grain boundaries in halide perovskites. Misorientation between two neighboring grains (grain boundary misorientation) can be quantified using the crystallographic misorientation angles and misorientation axes obtained using EBSD. The misorientation angle is the angle by which a grain is rotated, about the misorientation axis, such that the orientation of the transformed grain matches the neighboring grain after transformation. Figure 2D shows the grain boundary network and their respective misorientation angles between neighboring grains. The misorientation angle/axis statistics (Figures S12 and S13) demonstrate the presence of high angle grain boundaries with high frequency and strong preferred orientation of misorientation axis along the [110] direction. Importantly, Figure 2D shows that different grain boundaries have different misorientation and, therefore, may have different properties. In other words, these films exhibit a range of different grain boundaries, which might be expected to exhibit different properties. As stated earlier, understanding grain boundary properties has been critical to the development of many other photovoltaic semiconductor technologies, such as CdTe, GaAs, InP, and $Cu(In_{1-x}Ga_x)Se_2$,[22–29] and indeed other materials, such as high-temperature polycrystalline superconductors.[45,46] We anticipate that understanding the nature of the different grain boundaries identified by EBSD will be critical to understanding the properties of halide perovskite
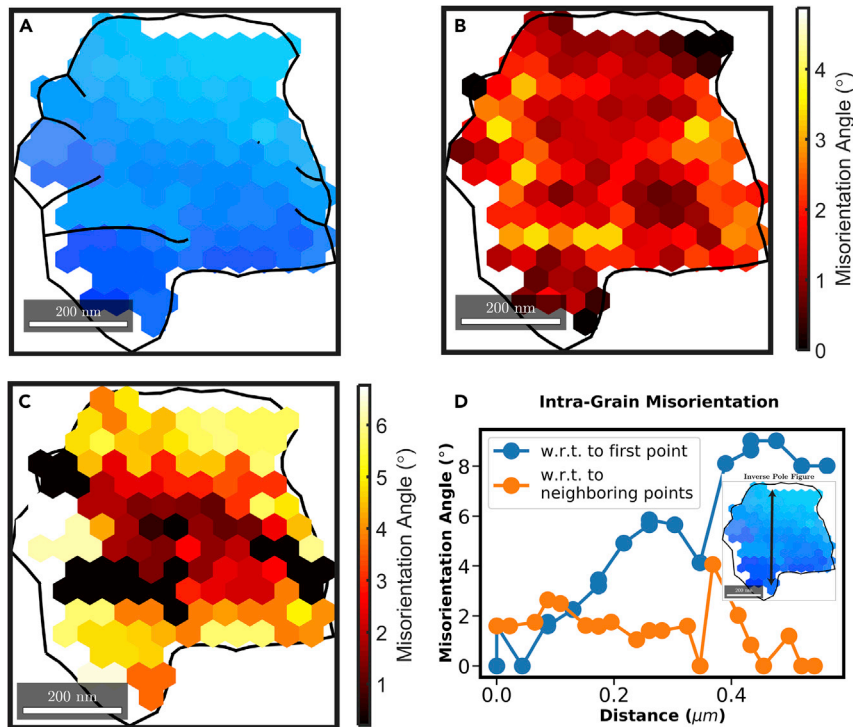
**Figure 3. Sub-grain Boundaries and Intra-grain Misorientation**

(A) Inverse pole figure (IPF) of an individual grain in a $CH_3NH_3PbI_3$ thin film with sub-grain boundaries. The outer black lines represent the outer grain boundary (i.e., with other grains), and the inner black lines represent the sub-grain boundaries. The IPF color key is the same as in Figures 1 and 2. The grains are identified using 4° as the threshold.

(B) Kernel average misorientation (KAM) showing the degree of misorientation between neighboring pixels within the grain.

(C) Misorientation with respect to mean orientation of the grain showing the local orientation heterogeneity in the grain.

(D) Plot of misorientation angle as a function of distance along the black arrow in the IPF in the inset. Blue circles denote the misorientation of each point with respect to the first point along the black arrow, and orange circles denote the misorientation of each point with respect to its neighboring points along the arrow.

photovoltaics,[21] and we speculate that properties such as anisotropic charge carrier transport across grain boundaries observed in halide perovskites[13,47–49] could depend on grain boundary properties such as misorientation angle, type of boundary, and the boundary interface energy.

Next, to investigate the structural heterogeneity at a sub-grain level in more detail, we examine crystal orientations within an individual grain. Due to high coefficient of thermal expansion anisotropy in tetragonal $CH_3NH_3PbI_3$, phase transition from cubic to tetragonal $CH_3NH_3PbI_3$ during film formation can introduce a significant amount of local residual stresses in the material.[50,51] These micro-stresses may be concentrated at the grain boundaries and sub-grain boundaries within the grain. Figure 3A shows the IPF of an individual grain from a $CH_3NH_3PbI_3$ film with sub-grain boundaries. The grains are identified using 4° as the threshold; however, the grain represented in Figure 3 is not affected by different thresholds (see Figure S14). Sub-grain boundaries have been shown to influence charge carrier recombination in other semiconductor photovoltaic technologies like GaAs and InP.[27,28] Recently, using optical microscopy, Li et al. suggested the presence of sub-grain special

## Joule

boundaries in large-grain $NH_2CHNH_2PbI_3$ thin films.[49] Here, we use crystallographic identification to unequivocally demonstrate the existence of sub-grain boundaries and precisely determine their location within the grain.

As stated earlier, local variations in lattice orientation can manifest as residual strain within the material.[50] Here, we analyze local variations in lattice orientations to infer the local strain within an individual grain. Kernel average misorientation (KAM) provides the average misorientation between a measurement point and its neighboring points.[43] In our case, it provides the average misorientation between each point and its six neighboring points within the same grain. We note that the KAM is a kernel or an individual measurement property where each point in the grain has a local misorientation value, whereas the previously described GOS is a grain property where the entire grain is assigned a local misorientation value. Figure 3B shows the KAM value calculated and plotted for each point within the grain. We observe KAM values as low as 0° and as high as 4.87° corresponding to low and high local misorientation regions, respectively. We note that the range of KAM values (0°–4.87°) observed here is within the same grain, demonstrating significant strain heterogeneity within an individual grain. Interestingly, the sub-grain boundaries (Figure 3A) are near regions with high KAM values (Figure 3B), consistent with the model that high misorientations within a grain will lead to sub-grain boundaries. Our observations show that local crystal misorientation generates the local strain heterogeneity observed within individual grains.

As evident from Figures 3A and 3B, the selected grain has a distribution of orientations within itself, exhibiting a GOS of 3.41°. Figure 3C shows the misorientation of individual measurement points within a grain with respect to the mean orientation of the grain. Regions near to the reference mean orientation have lower misorientation angles and vice versa. We observe higher misorientation angles with respect to mean orientation closer to the grain boundaries, suggesting a higher degree of lattice rotation or lattice bending near grain boundaries.

Figure 3D shows the plot of intra-grain misorientation angle as a function of distance within the grain, along the black arrow in the inset figure. Importantly, Figure 3D shows that the misorientation from one end of the grain to the other end can be as high as 9° (even though the grain boundaries were identified using a threshold of 4°). This result could indicate the possibility of variations in carrier transport both across and within an individual grain if the strain affects the local carrier mobility. We note that the sub-grain heterogeneity present in the grain shown in Figure 3 is representative of the population (see Figures S15 and S16 for SEM image of an individual grain along with sub-grain heterogeneity characterization and sub-grain heterogeneity in more grains from different films, respectively).

Finally, having quantified the local grain orientation spread, and hence the local strain, we use our high-resolution EBSD dataset to explore whether grain-to-grain variations in near-surface strain (Figure S17) could be sources of non-radiative recombination within the perovskite films. We expect the defects (and the strain) to be dominated by the surface, because surface-passivated halide perovskite thin films have demonstrated single-crystal-like quality.[4–6,52] To this end, we overlay the grain-boundary network obtained from grain identification onto the confocal photoluminescence (PL) image obtained on the same region (Figure 4A). The grain boundary network and the confocal PL image were aligned using an image registration program and fiducial marks created using atomic force microscope tip (see Note S2 for details).
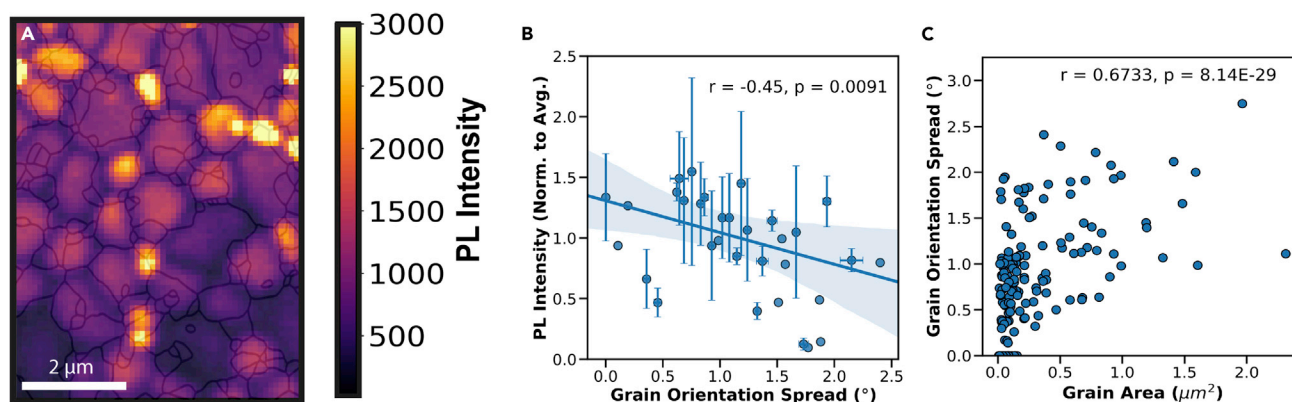
**Figure 4. Correlation between Local Luminescence, Orientation Heterogeneity, and Grain Area in CH$_3$NH$_3$PbI$_3$**

(A) Aligned confocal photoluminescence (PL) image and grain boundary network of the same region.

(B) Plot of PL intensity as a function of grain orientation spread (GOS) in CH$_3$NH$_3$PbI$_3$ showing negative correlation, with high statistical significance (p = 0.0091). The grains are binned in GOS intervals. The line represents a linear regression fit to the data with the shaded region representing a 95% confidence interval for the regression. Error bars represent the standard deviation of average PL intensity in a specific GOS interval.

(C) Plot of grain orientation spread as a function of grain area showing positive correlation, with high statistical significance (p = 8.14 × 10$^{-29}$). See Note S3 for discussion on p value and statistical significance.

To look for any relationship between local orientation heterogeneity and local non-radiative recombination, we plot photoluminescence intensity as a function of grain orientation spread. Our group has previously demonstrated that confocal PL maps, when measured at excitation densities below the local trap density ($\sim$10$^{15}$–10$^{17}$ cm$^{-3}$),[12,53–55] can reflect the local trap distribution in the film.[12,13] Although carrier diffusion is still important,[13,56] under such conditions, high PL intensities correspond to regions with lower trap density, and low PL intensities to regions with higher trap density.[13]

Here, we measure confocal PL maps at low incident excitation fluences of $\sim$0.2 µJ/cm$^2$ per pulse (at 470 nm with 1 MHz repetition rate) corresponding to an initial carrier excitation density of $\sim$10$^{16}$ cm$^{-3}$ and time-averaged carrier density of $\sim$10$^{15}$ cm$^{-3}$. Next, we measure the local crystal orientation across the same region using EBSD as demonstrated earlier. Using this approach, Figure 4B plots the normalized average PL intensity within a grain versus the grain orientation spread within the corresponding grain for more than 100 grains from different samples (see Figure S18 for correlation plots from individual sample sets). We find a negative correlation between the grain orientation spread and PL intensity with high statistical significance (p value = 0.0091; see Note S3 for more details on p value). In other words, the larger the grain orientation spread, the lower the PL intensity of the local perovskite. This result provides a direct link between local intra-grain strain and local nonradiative defect density by showing that grains with higher grain orientation spreads have lower PL intensity and, therefore, higher trap densities contributing to non-radiative recombination.

Figure 4C shows the relation between grain area and the corresponding orientation spread within the grain. We find a strong positive correlation between the grain area and grain orientation spread, with high statistical significance (p value = 8.14 × 10$^{-29}$). We note that this conclusion does not depend on the threshold value chosen during grain detection. In other words, we observe a strong positive correlation between grain area and grain orientation spread for all different grain threshold values (Figure S19). This means that, in the case of the samples measured

in this study, as the grain size increases the orientation spread (and hence, local strain) also increases. We note that at fluences used in this study (corresponding to trap densities in the film), we find very low anticorrelation (r = −0.2) between PL intensity and grain area (Figure S20), consistent with our previous observations.[13] Importantly, this result indicates that the correlation between PL and grain orientation spread shown in Figure 4B is not solely due to the relation between grain size and PL; instead, grain orientation spread appears to be more important than grain size.

## DISCUSSION

Notably, an increase in grain orientation spread (and local strain) with increasing grain area might help explain why some of the smaller grain films in the literature have shown higher PCE and why increasing apparent grain sizes, as imaged by SEM, has not always corroborated with increasing PCE.[57] Specifically, we speculate that smaller grain films studied to date may have less orientation spread and, thus, lower strain compared to large grains.

However, we emphasize that these results do not indicate researchers should necessarily aim to create perovskite films with smaller grains for solar cell applications. Grain boundaries and surface traps act as centers for non-radiative recombination in many materials, including halide perovskites.[5–7,12,13,21,53,58–65] Instead, the point we are making is that local crystal orientation is also important, perhaps more so than grain size in some films. Ideally, we would want films with larger grain sizes and low orientation spread within a grain, i.e., highly oriented and low strain. Promisingly, Choi and co-workers recently demonstrated that perovskite thin films with higher degrees of orientation can be achieved at the lab scale.[66,67] As lab-scale deposition techniques are translated to large-scale deposition methods such as roll-to-roll printing, spray coating, and slot die coating,[68,69] our results, and the general methods herein, provide insight for optimizing deposition conditions and suggest a need for orientation and strain engineering.[70]

In conclusion, we demonstrate local crystal orientation maps of archetypal $CH_3NH_3PbI_3$ perovskite thin films, most commonly investigated for solar cell applications, generated using the state-of-the-art EBSD detector with high sensitivity and fast readout. We show that while SEM morphology is generally consistent with EBSD, there are features in the film that are only visible in EBSD, and therefore, SEM morphology alone is insufficient to identify grains and grain boundaries. In addition to providing true grain sizes for halide perovskites, orientation imaging using EBSD also allows us to probe the crystallographic nature of the film. We observe local crystal orientation heterogeneity within individual grains throughout the thin film and find that the orientation heterogeneity varies from grain to grain. Our results demonstrate that although a grain is defined as a unit of microstructure with a single orientation, in reality, in perovskites a grain has an average orientation with significant orientational spread or heterogeneity that contributes to the local strain within the grain. We propose that such orientational heterogeneity within grains could be a result of heterogeneous nucleation and growth, variations in local concentration gradients,[71] and/or phase transitions post-annealing.[37,50,51,72,73] Next, by studying the crystallographic nature of grain boundaries, we show that there are a range of different grain boundary misorientations, and therefore, different grain boundaries will have different properties such as carrier transport, interface energy, etc. Using EBSD, we also demonstrate the presence of sub-grain boundaries formed near regions of high local crystal misorientation. We observed

misorientations as high as 9° from one end of the grain to another. Finally, we use correlated confocal PL microscopy and EBSD to understand the relationship between local crystal orientation heterogeneity and local non-radiative recombination, as it relates directly to photovoltaic performance. We observe low PL intensity (high non-radiative recombination) in regions with high grain orientation spreads (high strain regions) and high PL intensity (low non-radiative recombination) in regions with low grain orientation spreads (low strain regions). Furthermore, we observe that the orientation spread increases with increasing grain sizes. Our results point toward the need to understand and control the local crystal orientation by engineering deposition protocols that provide large grains with low orientation heterogeneity (lower strain). These results provide critical insight into the interplay between local crystal orientation heterogeneity and local non-radiative recombination and further our understanding of the local structure-function interplay in halide perovskite thin films for photovoltaics.

## EXPERIMENTAL PROCEDURES

### Precursor Preparation and Film Deposition

In a nitrogen-filled glovebox, a methylammonium iodide (MAI) solution (1.78 M) was made by dissolving MAI (Dyesol, CAS:14965-49-2) in anhydrous N,N-dimethylformamide (DMF). Lead acetate trihydrate (PbOAc$_2$ ·3H$_2$O) (99.999%, Sigma-Aldrich, CAS:6080-56-4) was added to the MAI solution at a 3:1 molar ratio of MAI to PbOAc$_2$ ·3H$_2$O (0.59 M). A hypophosphorous acid (HPA) solution was further added to the precursor solution with a molar ratio HPA/PbOAc2·3H2O of 8%.[35]

Glass substrates were cleaned by sequentially sonicating in 2% Micro-90 detergent, DI water, acetone, then propan-2-ol. Prior to film deposition, the glass substrates were plasma-cleaned. The perovskite precursor solution was spin-coated on top in a nitrogen-filled glovebox, at 2,000 rpm for 45 s to form the perovskite thin film layer. The films were then annealed at room temperature for 10 min and at 100°C for 5 min.

### Fluorescence Lifetime Imaging Microscopy

A custom scanning confocal microscope built around Nikon TE-2000 inverted microscope with a sample stage controlled by Physik Instrumente E-710 piezo controller was used to measure fluorescence images. The system was first calibrated using 200 nm fluorescent microspheres (Lifetechnologies FluoSpheres Polystyrene Microspheres, 200 nm, red fluorescent, 580/605 nm). The sample was illuminated through a LU Nikon Plan Fluor 100× infinity corrected dry objective (0.9 NA), with 470 nm pulsed diode laser (PDL-800 LDH-P-C-470B, 1 MHz, ~300 ps pulse width), and the emission was filtered using a 50/50 dichroic beam splitter and a pair of 500/600 nm long-pass filters. The local fluorescence was measured by directing the emission to a Micro Photon Devices PDM series single-photon avalanche photodiode with a 50 μm active area. The pixel size (or scanning step size) used for fluorescence lifetime images was 100 nm, and the pixel dwell time (or integration time) was 100 ms.

### Electron Back-Scatter Diffraction (EBSD)

PELCO conductive silver paint was first deposited on top of the perovskite film on glass to cover all the edges of the film. Upon drying, it forms a thick silver layer around edges to provide good conductivity with a sheet resistance of 0.066 ohm/sq. The dried silver paint was then connected to a metal sample holder for further grounding. EBSD was performed in the region between the silver paint (~5 × 5 mm) to avoid any charging effects. The electron beam was optimized to 100 pA beam current and 6 kV accelerating voltage with a 10 mm working distance

# Joule

to the sample. The sample was tilted such that the electron beam was hitting the sample at 70° with respect to the sample surface normal. The electron beam was scanned across the sample with a step size of 50–100 nm to collect Kikuchi patterns at every pixel. The patterns were collected using EDAX OIM software, and the pixel integration time was 100 ms. The electron dose rate for the measurement was estimated to be $\sim 0.1$ electrons/$\text{Å}^2$ per s. The total dose for $8 \times 8$ μm scan with 0.1 μm step size and 100 ms pixel dwell time was estimated to be $\sim 62$ electrons/$\text{Å}^2$. The 1/e decay length for the backscatter electron energy distribution in the X-Y plane is $\sim 106$ nm (Figure S17), thus justifying the assumption in the calculation that the beam size is similar to the step size in the measurement.

## SUPPLEMENTAL INFORMATION

Supplemental Information can be found online at https://doi.org/10.1016/j.joule.2019.09.001.

## AUTHOR CONTRIBUTIONS

S.J. fabricated the films for confocal PL imaging and EBSD, carried out the PL experiments, analyzed the EBSD and PL results, and coordinated the experiments under the supervision of D.S.G. H.S., G.W.P.A., A.L., and L.A.M. carried out the EBSD measurements and indexing under the supervision of E.C.G. and B.E. D.S.G. and S.J. conceived the idea, designed the experiments, interpreted the results, and wrote the manuscript. All authors contributed to the editing of the manuscript.

## DECLARATION OF INTERESTS

The EBSD detector used in this study is now being commercialized by Amsterdam Scientific Instruments.

## REFERENCES

1. National Renewable Energy Laboratory Efficiency Chart (2019). https://www.nrel.gov/pv/assets/pdfs/pv-efficiency-chart.20190103.pdf (accessed February 1, 2019).

2. Pazos-Outón, L.M., Xiao, T.P., and Yablonovitch, E. (2018). Fundamental Efficiency Limit of Lead Iodide Perovskite Solar Cells. J. Phys. Chem. Lett. 9, 1703–1711.

3. Hörantner, M.T., and Snaith, H.J. (2017). Predicting and optimising the energy yield of perovskite-on-silicon tandem solar cells under real world conditions. Energy Environ. Sci. 10, 1983–1993.

4. Braly, I.L., Dequilettes, D.W., Pazos-Outón, L.M., Burke, S., Ziffer, M.E., Ginger, D.S., and Hillhouse, H.W. (2018). Hybrid perovskite films

approaching the radiative limit with over 90% photoluminescence quantum efficiency. Nat. Photonics 12, 355–361.

5. deQuilettes, D.W., Koch, S., Burke, S., Paranji, R., Shropshire, A.J., Ziffer, M.E., and Ginger, D.S. (2016a). Photoluminescence Lifetimes Exceeding 8 μs and Quantum Yields Exceeding 30% in Hybrid Perovskite Thin Films

# Joule

**CellPress**

by Ligand Passivation. ACS Energy Lett. 1, 438–444.

6. Brenes, R., Guo, D., Osherov, A., Noel, N.K., Eames, C., Hutter, E.M., Pathak, S.K., Niroui, F., Friend, R.H., Islam, M.S., et al. (2017). Metal Halide Perovskite Polycrystalline Films Exhibiting Properties of Single Crystals. Joule 1, 155–167.

7. Stavrakas, C., Zhumekenov, A.A., Brenes, R., Abdi-Jalebi, M., Bulović, V., Bakr, O.M., Barnard, E.S., and Stranks, S.D. (2018). Probing buried recombination pathways in perovskite structures using 3D photoluminescence tomography. Energy Environ. Sci. 11, 2846–2852.

8. Wang, J., Fu, W., Jariwala, S., Sinha, I., Jen, A.K.-Y., and Ginger, D.S. (2018b). Reducing Surface Recombination Velocities at the Electrical Contacts Will Improve Perovskite Photovoltaics. ACS Energy Lett. 4, 222–227.

9. Stolterfoht, M., Caprioglio, P., Wolff, C.M., Márquez, J.A., Nordmann, J., Zhang, S., et al. (2018). The perovskite/transport layer interfaces dominate non-radiative recombination in efficient perovskite solar cells. arXiv, arXiv:1810.01333. https://arxiv.org/abs/1810.01333.

10. Schnitzer, I., Yablonovitch, E., Caneau, C., and Gmitter, T.J. (1993). Ultrahigh spontaneous emission quantum efficiency, 99.7% internally and 72% externally, from AlGaAs/GaAs/AlGaAs double heterostructures. Appl. Phys. Lett. 62, 131–133.

11. Abdi-Jalebi, M., Andaji-Garmaroudi, Z., Cacovich, S., Stavrakas, C., Philippe, B., Richter, J.M., Alsari, M., Booker, E.P., Hutter, E.M., Pearson, A.J., et al. (2018). Maximizing and stabilizing luminescence from halide perovskites with potassium passivation. Nature 555, 497–501.

12. deQuilettes, D.W., Vorpahl, S.M., Stranks, S.D., Nagaoka, H., Eperon, G.E., Ziffer, M.E., Snaith, H.J., and Ginger, D.S. (2015). Solar cells. Impact of microstructure on local carrier lifetime in perovskite solar cells. Science 348, 683–686.

13. deQuilettes, D.W., Jariwala, S., Burke, S., Ziffer, M.E., Wang, J.T.W., Snaith, H.J., and Ginger, D.S. (2017). Tracking Photoexcited Carriers in Hybrid Perovskite Semiconductors: Trap-Dominated Spatial Heterogeneity and Diffusion. ACS Nano 11, 11488–11496.

14. Yun, J.S., Ho-Baillie, A., Huang, S., Woo, S.H., Heo, Y., Seidel, J., Huang, F., Cheng, Y.B., and Green, M.A. (2015). Benefit of grain boundaries in organic-inorganic halide planar perovskite solar cells. J. Phys. Chem. Lett. 6, 875–880.

15. Yang, M., Zeng, Y., Li, Z., Kim, D.H., Jiang, C.-S., van de Lagemaat, J., and Zhu, K. (2017a). Do grain boundaries dominate non-radiative recombination in CH₃NH₃PbI₃ perovskite thin films? Phys. Chem. Chem. Phys. 19, 5043–5050.

16. Zhou, Y., Game, O.S., Pang, S., and Padture, N.P. (2015). Microstructures of Organometal Trihalide Perovskites for Solar Cells: Their Evolution from Solutions and Characterization. J. Phys. Chem. Lett. 6, 4827–4839.

17. Dr. Joseph J. Berry, National Renewable Energy Laboratory [@joe_jberry] (June 30, 2018) [Tweet] n.d., accessed February 12, 2019.

18. Xiao, C., Li, Z., Guthrey, H., Moseley, J., Yang, Y., Wozny, S., Moutinho, H., To, B., Berry, J.J., Gorman, B., et al. (2015). Mechanisms of Electron-Beam-Induced Damage in Perovskite Thin Films Revealed by Cathodoluminescence Spectroscopy. J. Phys. Chem. C 119, 26904–26911.

19. Rothmann, M.U., Li, W., Zhu, Y., Liu, A., Ku, Z., Bach, U., Etheridge, J., and Cheng, Y.-B. (2018). Structural and Chemical Changes to CH₃NH₃PbI₃ Induced by Electron and Gallium Ion Beams. Adv. Mater. 30, e1800629.

20. Leonhard, T., Schulz, A., Röhm, H., Wagner, S., Altermann, F.J., Rheinheimer, W., Hoffmann, M.J., and Colsmann, A. (2019). Probing the Microstructure of Methylammonium Lead Iodide Perovskite Solar Cells. Energy Technol. (Weinheim) 7, 1800989.

21. Adhyaksa, G.W.P., Brittman, S., Āboliņš, H., Lof, A., Li, X., Keelor, J.D., Luo, Y., Duevski, T., Heeren, R.M.A., Ellis, S.R., et al. (2018). Understanding Detrimental and Beneficial Grain Boundary Effects in Halide Perovskites. Adv. Mater. 30, e1804792.

22. Kawamura, M., Yamada, T., Suyama, N., Yamada, A., and Konagai, M. (2010). Grain boundary evaluation of Cu(In1-xGax)Se 2solar cells. Jpn. J. Appl. Phys. 49, 0623011–0623013.

23. Walls, J.M., Abbas, A., West, G.D., Bowers, J.W., Isherwood, P.J.M., Kaminski, P.M., Maniscalco, B., Sampath, W.S., and Barth, K.L. (2013). The effect of annealing treatments on close spaced sublimated cadmium telluride thin film solar cells. In Materials Research Society Symposium Proceedings (IEEE), pp. 147–152.

24. Stoffers, A., Cojocaru-Mirédin, O., Seifert, W., Zaefferer, S., Riepe, S., and Raabe, D. (2015). Grain boundary segregation in multicrystalline silicon: Correlative characterization by EBSD, EBIC, and atom probe tomography. Prog. Photovolt. Res. Appl. 23, 1742–1753.

25. Poplawsky, J.D., Paudel, N.R., Li, C., Parish, C.M., Leonard, D., Yan, Y., and Pennycook, S.J. (2014). Direct Imaging of Cl- and Cu-Induced Short-Circuit Efficiency Changes in CdTe Solar Cells. Adv. Energy Mater. 4, 1400454.

26. Nichterwitz, M., Abou-Ras, D., Sakurai, K., Bundesmann, J., Unold, T., Scheer, R., and Schock, H.W. (2009). Influence of grain boundaries on current collection in Cu(In,Ga)Se2thin-film solar cells. Thin Solid Films 517, 2554–2557.

27. Brown, E., Sheng, C., Shimamura, K., Shimojo, F., and Nakano, A. (2015). Enhanced charge recombination due to surfaces and twin defects in GaAs nanostructures. J. Appl. Physiol. 117, 054307.

28. Woo, R.L., Xiao, R., Kobayashi, Y., Gao, L., Goel, N., Hudait, M.K., Mallouk, T.E., and Hicks, R.F. (2008). Effect of twinning on the photoluminescence and photoelectrochemical properties of indium phosphide nanowires grown on silicon (111). Nano Lett. 8, 4664–4669.

29. Abou-Ras, D., and Pantleon, K. (2007). The impact of twinning on the local texture of chalcopyrite-type thin films. Phys. Status Solidi Rapid Res. Lett. 1, 187–189.

30. Saliba, M., Correa-Baena, J.-P., Grätzel, M., Hagfeldt, A., and Abate, A. (2018). Perovskite Solar Cells: From the Atomic Level to Film Quality and Device Performance. Angew. Chem. Int. Ed. Engl. 57, 2554–2569.

31. Leblebici, S.Y., Leppert, L., Li, Y., Reyes-Lillo, S.E., Wickenburg, S., Wong, E., Lee, J., Melli, M., Ziegler, D., Angell, D.K., et al. (2016). Facet-dependent photovoltaic efficiency variations in single grains of hybrid halide perovskite. Nat. Energy 1, 16093.

32. Guo, Z., Manser, J.S., Wan, Y., Kamat, P.V., and Huang, L. (2015). Spatial and temporal imaging of long-range charge transport in perovskite thin films by ultrafast microscopy. Nat. Commun. 6, 7471.

33. Nishikawa, S., and Kikuchi, S. (1928). Diffraction of Cathode Rays by Mica. Nature 121, 1019–1020.

34. Levine, E., Bell, W.L., and Thomas, G. (1966). Further applications of Kikuchi diffraction patterns; Kikuchi maps. J. Appl. Physiol. 37, 2141–2148.

35. Zhang, W., Saliba, M., Moore, D.T., Pathak, S.K., Hörantner, M.T., Stergiopoulos, T., Stranks, S.D., Eperon, G.E., Alexander-Webber, J.A., Abate, A., et al. (2015). Ultrasmooth organic-inorganic perovskite thin-film formation and crystallization for efficient planar heterojunction solar cells. Nat. Commun. 6, 6142.

36. Poglitsch, A., and Weber, D. (1987). Dynamic disorder in methylammoniumtrihalogenoplumbates (II) observed by millimeter-wave spectroscopy. J. Chem. Phys. 87, 6373–6378.

37. Baikie, T., Fang, Y., Kadro, J.M., Schreyer, M., Wei, F., Mhaisalkar, S.G., Gratzel, M., and White, T.J. (2013). Synthesis and crystal chemistry of the hybrid perovskite (CH3NH3)PbI3 for solid-state sensitised solar cell applications. J. Mater. Chem. A Mater. Energy Sustain. 1, 5628.

38. Jones, T.W., Osherov, A., Alsari, M., Sponseller, M., Duck, B.C., Jung, Y.-K., Settens, C., Niroui, F., Brenes, R., Stan, C., et al. (2019). Lattice Strain Causes Non-Radiative Losses in Halide Perovskites. Energy Environ. Sci. 12, 596–606.

39. Rothmann, M.U., Li, W., Etheridge, J., and Cheng, Y.-B. (2017a). Microstructural Characterisations of Perovskite Solar Cells - From Grains to Interfaces: Techniques, Features, and Challenges. Adv. Energy Mater. 7, 1700912.

40. Bachmann, F., Hielscher, R., and Schaeben, H. (2011). Grain detection from 2d and 3d EBSD data–specification of the MTEX algorithm. Ultramicroscopy 111, 1720–1733.

41. Kunze, K., Wright, S.I., Adams, B.L., and Dingley, D.J. (1993). Advances in automatic EBSP single orientation measurements. Textures Microstruct. 20, 41–54.

42. Bachmann, F., Hielscher, R., Jupp, P.E., Pantleon, W., Schaeben, H., and Wegert, E. (2010). Inferential statistics of electron backscatter diffraction data from within individual crystalline grains. J. Appl. Cryst. 43, 1338–1355.

https://twitter.com/joe_jberry/status/1013192769316139008.

# Joule

# CellPress

43. Wright, S.I., Nowell, M.M., and Field, D.P. (2011). A review of strain analysis using electron backscatter diffraction. Microsc. Microanal. *17*, 316–329.

44. Stoneham, A.M. (1981). Non-radiative transitions in semiconductors. Rep. Prog. Phys. *44*, 1251–1295.

45. Klie, R.F., Buban, J.P., Varela, M., Franceschetti, A., Jooss, C., Zhu, Y., Browning, N.D., Pantelides, S.T., and Pennycook, S.J. (2005). Enhanced current transport at grain boundaries in high-T(c) superconductors. Nature *435*, 475–478.

46. Dimos, D., Chaudhari, P., and Mannhart, J. (1990). Superconducting transport properties of grain boundaries in YBa2Cu3O7 bicrystals. Phys. Rev. B Condens. Matter *41*, 4038–4049.

47. Snaider, J.M., Guo, Z., Wang, T., Yang, M., Yuan, L., Zhu, K., and Huang, L. (2018). Ultrafast Imaging of Carrier Transport across Grain Boundaries in Hybrid Perovskite Thin Films. ACS Energy Lett. *3*, 1402–1408.

48. Delor, M., Weaver, H.L., Yu, Q., and Ginsberg, N.S. (2018). Universal imaging of material functionality through nanoscale tracking of energy flow. arXiv, arXiv:1805.09982. https://arxiv.org/abs/1805.09982.

49. Li, W., Yadavalli, S.K., Lizarazo-Ferro, D., Chen, M., Zhou, Y., Padture, N.P., and Zia, R. (2018). Subgrain special boundaries in halide perovskite thin films restrict carrier diffusion. ACS Energy Lett. *3*, 2669–2670.

50. Ramirez, C., Yadavalli, S.K., Garces, H.F., Zhou, Y., and Padture, N.P. (2018). Thermo-mechanical behavior of organic-inorganic halide perovskites for solar cells. Scr. Mater. *150*, 36–41.

51. Rolston, N., Bush, K.A., Printz, A.D., Gold-Parker, A., Ding, Y., Toney, M.F., McGehee, M.D., and Dauskardt, R.H. (2018). Engineering Stress in Perovskite Solar Cells to Improve Stability. Adv. Energy Mater. *8*, 1802139.

52. Noel, N.K., Abate, A., Stranks, S.D., Parrott, E.S., Burlakov, V.M., Goriely, A., and Snaith, H.J. (2014). Enhanced photoluminescence and solar cell performance via Lewis base passivation of organic-inorganic lead halide perovskites. ACS Nano *8*, 9815–9821.

53. deQuilettes, D.W., Zhang, W., Burlakov, V.M., Graham, D.J., Leijtens, T., Osherov, A., Bulović, V., Snaith, H.J., Ginger, D.S., and Stranks, S.D. (2016c). Photo-induced halide redistribution in organic-inorganic perovskite films. Nat. Commun. *7*, 11683.

54. Stranks, S.D., Burlakov, V.M., Leijtens, T., Ball, J.M., Goriely, A., and Snaith, H.J. (2014). Recombination Kinetics in Organic-Inorganic Perovskites: Excitons, Free Charge, and Subgap States. Phys. Rev. Appl. *2*, 034007.

55. Herz, L.M. (2016). Charge-Carrier Dynamics in Organic-Inorganic Metal Halide Perovskites. Annu. Rev. Phys. Chem. *67*, 65–89.

56. Tian, W., Cui, R., Leng, J., Liu, J., Li, Y., Zhao, C., Zhang, J., Deng, W., Lian, T., and Jin, S. (2016). Limiting Perovskite Solar Cell Performance by Heterogeneous Carrier Extraction. Angew. Chem. Int. Ed. Engl. *55*, 13067–13071.

57. Wang, F., Bai, S., Tress, W., Hagfeldt, A., and Gao, F. (2018a). Defects engineering for high-performance perovskite solar cells. Npj Flex. Electron. *2*, 22.

58. Simpson, M.J., Doughty, B., Das, S., Xiao, K., and Ma, Y.Z. (2017). Separating Bulk and Surface Contributions to Electronic Excited-State Processes in Hybrid Mixed Perovskite Thin Films via Multimodal All-Optical Imaging. J. Phys. Chem. Lett. *8*, 3299–3305.

59. Yamashita, D., Handa, T., Ihara, T., Tahara, H., Shimazaki, A., Wakamiya, A., and Kanemitsu, Y. (2016). Charge Injection at the Heterointerface in Perovskite CH3NH3PbI3 Solar Cells Studied by Simultaneous Microscopic Photoluminescence and Photocurrent Imaging Spectroscopy. J. Phys. Chem. Lett. *7*, 3186–3191.

60. Eperon, G.E., Moerman, D., and Ginger, D.S. (2016). Anticorrelation between Local Photoluminescence and Photocurrent Suggests Variability in Contact to Active Layer in Perovskite Solar Cells. ACS Nano *10*, 10258–10266.

61. Moerman, D., Eperon, G.E., Precht, J.T., and Ginger, D.S. (2017). Correlating Photoluminescence Heterogeneity with Local Electronic Properties in Methylammonium Lead Tribromide Perovskite Thin Films. Chem. Mater. *29*, 5484–5492.

62. Brenes, R., Eames, C., Bulović, V., Islam, M.S., and Stranks, S.D. (2018). The Impact of Atmosphere on the Local Luminescence Properties of Metal Halide Perovskite Grains. Adv. Mater. *30*, e1706208.

63. Bischak, C.G., Sanehira, E.M., Precht, J.T., Luther, J.M., and Ginsberg, N.S. (2015). Heterogeneous Charge Carrier Dynamics in Organic-Inorganic Hybrid Materials: Nanoscale Lateral and Depth-Dependent Variation of Recombination Rates in Methylammonium Lead Halide Perovskite Thin Films. Nano Lett. *15*, 4799–4807.

64. Draguta, S., Thakur, S., Morozov, Y.V., Wang, Y., Manser, J.S., Kamat, P.V., and Kuno, M. (2016). Spatially Non-uniform Trap State Densities in Solution-Processed Hybrid Perovskite Thin Films. J. Phys. Chem. Lett. *7*, 715–721.

65. Vrućinić, M., Matthiesen, C., Sadhanala, A., Divitini, G., Cacovich, S., Dutton, S.E., Ducati, C., Atatüre, M., Snaith, H., Friend, R.H., et al. (2015). Local Versus Long-Range Diffusion Effects of Photoexcited States on Radiative Recombination in Organic-Inorganic Lead Halide Perovskites. Adv. Sci. (Weinh.) *2*, 1500136.

66. Foley, B.J., Cuthriell, S., Yazdi, S., Chen, A.Z., Guthrie, S.M., Deng, X., Giri, G., Lee, S.-H., Xiao, K., Doughty, B., et al. (2018). Impact of Crystallographic Orientation Disorders on Electronic Heterogeneities in Metal Halide Perovskite Thin Films. Nano Lett. *18*, 6271–6278.

67. Chen, A.Z., Foley, B.J., Ma, J.H., Alpert, M.R., Niezgoda, J.S., and Choi, J.J. (2017). Crystallographic orientation propagation in metal halide perovskite thin films. J. Mater. Chem. A Mater. Energy Sustain. *5*, 7796–7800.

68. Dou, B., Whitaker, J.B., Bruening, K., Moore, D.T., Wheeler, L.M., Ryter, J., Breslin, N.J., Berry, J.J., Garner, S.M., Barnes, F.S., et al. (2018). Roll-to-Roll Printing of Perovskite Solar Cells. ACS Energy Lett. *3*, 2558–2565.

69. Yang, M., Li, Z., Reese, M.O., Reid, O.G., Kim, D.H., Siol, S., Klein, T.R., Yan, Y., Berry, J.J., Van Hest, M.F.A.M., et al. (2017). Perovskite ink with wide processing window for scalable high-efficiency solar cells. Nat. Energy *2*, 17038.

70. Zhu, C., Niu, X., Fu, Y., Li, N., Hu, C., Chen, Y., He, X., Na, G., Liu, P., Zai, H., et al. (2019). Strain engineering in perovskite solar cells and its impacts on carrier dynamics. Nat. Commun. *10*, 815.

71. Hu, Q., Zhao, L., Wu, J., Gao, K., Luo, D., Jiang, Y., Zhang, Z., Zhu, C., Schaible, E., Hexemer, A., et al. (2017). In situ dynamic observations of perovskite crystallisation and microstructure evolution intermediated from [PbI 6 ]4- cage nanoparticles. Nat. Commun. *8*, 15688.

72. Vorpahl, S.M., Giridharagopal, R., Eperon, G.E., Hermes, I.M., Weber, S.A.L., and Ginger, D.S. (2018). Orientation of Ferroelectric Domains and Disappearance upon Heating Methylammonium Lead Triiodide Perovskite from Tetragonal to Cubic Phase. ACS Appl. Energy Mater. *1*, 1534–1539.

73. Rothmann, M.U., Li, W., Zhu, Y., Bach, U., Spiccia, L., Etheridge, J., and Cheng, Y.-B. (2017b). Direct observation of intrinsic twin domains in tetragonal CH₃NH₃PbI₃. Nat. Commun. *8*, 14547.

# Supplemental Information

# Local Crystal Misorientation Influences

# Non-radiative Recombination

# in Halide Perovskites

Sarthak Jariwala, Hongyu Sun, Gede W.P. Adhyaksa, Andries Lof, Loreta A. Muscarella, Bruno Ehrler, Erik C. Garnett, and David S. Ginger

**Note S1.**

**Electron Back-Scatter Diffraction (EBSD)**

The individual Kikuchi patterns acquired from EBSD were indexed to a tetragonal MAPI structure with I4/mcm space group symmetry.[1,2] The lattice parameters used were a = b = 8.84 Å and c = 12.63 Å. The overall absolute error in orientation determination was calculated using average fit to be 1.8° (typically, the accuracy of absolute orientation determination is ~2°).[3] Average fit describes the average angular difference between the detected Kikuchi bands in the diffraction pattern and the corresponding bands reconstructed from the orientation solution.[4] The average fit value is heavily dependent on the pattern quality and the Kikuchi band detection parameters.[5] However, when detecting sub-grain microstructures, the accuracy of relative orientations between adjacent data points is more important.[3] The relative angular resolution was measured by scanning across a Si (100) single crystal. The orientation noise or the angular resolution was found to be <1° for 90% of the points. The beam conditions were 6 kV accelerating voltage, 800 pA beam current and 0.2 s exposure.

Post indexing, the EBSD data was analyzed and plotted using MTEX, an open-source MATLAB toolbox for texture/orientation analysis.[6,7]

**Kikuchi Diffraction Patterns Analysis**

We process the data using a home script to remove background, optimize brightness and contrast, and balance the signal in 4 quadrants of the detector. The boundaries between the 4 quadrants of the detector are also removed to prevent it from being recognized as a diffraction line. Using OIM Analysis Software from EDAX, the patterns are corrected to reduce the noise levels using Neighbor Pattern Averaging & Reindexing (NPAR) method prior to indexing.

The Kikuchi patterns are also calibrated with an Aluminum metal sheet at the same working distance as the perovskite sample. Next, we optimize Hough transform by adjusting convolution mask, maximum band count, Rho fraction. After indexing, we correct pseudosymmetry and correct non-indexed points with grain dilation function. Lastly, we further improve image with Neighbor Orientation Correlation.

**Grain Detection using MTEX**
During grain identification from raw inverse pole figure (IPF), pixelated regions are first identified and removed. These are the points that the grain detection algorithm identifies as one pixel grain, and since that is likely a random measurement point/indexing error, they are removed from the map.
Once these pixels are removed from the EBSD map, a grain threshold angle is selected, and grain identification is performed using MTEX texture analysis package. According to the MTEX algorithm,[8] missing data due to measurement errors (here the removed pixels) do not interfere in the grain detection process.[8] Briefly, in the MTEX algorithm, there is no systemic bias in the assignment of these missing orientations and, they do not cause the grain to be split into different grains. The missing orientation data are equally assigned to neighboring points.

Importantly, since the pixels are removed, they do not contribute to or interfere in any further analysis of grains, grain boundaries, grain orientation spread, etc.

Post grain detection, we plot the mean grain orientation along with the grain boundaries. The above process is depicted in Figure S8.

**Note S2.**

**Aligning Confocal Photoluminescence (PL) Images and EBSD maps**

First, a region of interest (ROI) was formed by using Atomic Force Microscope (AFM) tip in contact mode to precisely scratch through the perovskite film. The ROI size was defined by AFM controls in x and y direction. After ROI was formed, confocal PL was performed on the ROI and silver paint was then deposited on the sides of the film for EBSD. Then, EBSD was performed on the same ROI to generate a local crystal orientation map.

Using an image registration program written in python using packages such as scikit-image[9] and OpenCV, the confocal PL maps and EBSD maps were aligned keeping ROI fiducial markers as known reference points across the two maps. Image registration between PL and EBSD was achieved by using fiducial markers followed by affine transformation (to account for resolution differences, beam angle etc). Post alignment, the PL and EBSD were overlaid to map the grain orientation spread of the grains to their corresponding local PL. Since the analysis requires correlation with PL, grains that were not optically resolved (smaller than the resolution limit of the microscope) were not considered for the analysis. Furthermore, grains right beside the scratch were also not considered for the analysis due to possible mechanical damage from scratching. The data were binned in intervals of GOS to create a plot of average PL intensity as a function of GOS.

**Note S3.**

**Hypothesis testing and p-value**

In inferential statistics, hypothesis testing is used to deduce relationships between the underlying distributions. The most common test is the null hypothesis ($H_0$) versus the alternate hypothesis ($H_a$) test. $H_0$ assumes that there is no relationship between underlying distributions, say X and Y. $H_a$ assumes that there is some relationship between the distributions.[10]

The p-value is the probability of the occurrence of a given event within a statistical hypothesis test. In other words, the p-value indicates the probability of uncorrelated distributions (X and Y) producing the same correlation as determined from the correlated distributions, X and Y.

The interpretation of p-value is as follows: a small p-value (generally, $p<0.05$ or 5%) indicates that it is *unlikely* that any association between the distributions (X & Y) exists due to *random chance*. Therefore, if we see a small p-value ($p<0.05$), we can infer that there is a relationship between the distributions, and we can reject the null hypothesis. In other words, a small p-value ($p<0.05$) indicates that there is statistically significant relationship between X and Y.[10] On

the contrary, if the p-value is greater than 0.05, we can infer that the relationship between the distributions is not statistically significant and we cannot reject the null hypothesis.[10] We note that a p-value larger than the threshold (0.05) does not imply there is simply *no relationship* between the distributions. But, instead, the hypothesis under investigation does not adequately explain the observations.
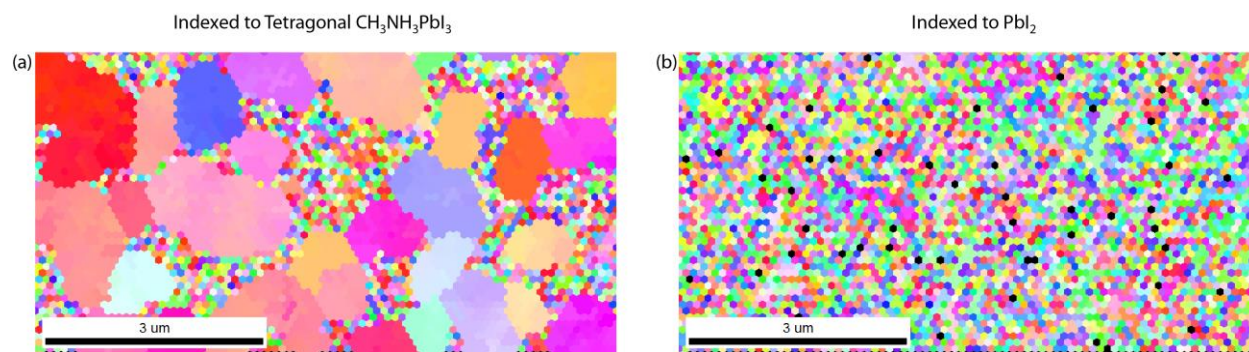
We also note that although the choice of p-value threshold of 0.05 is most commonly used, it is an arbitrary convention.

The correlations and p-values were calculated using scipy (scipy.stats) library in python.[11]
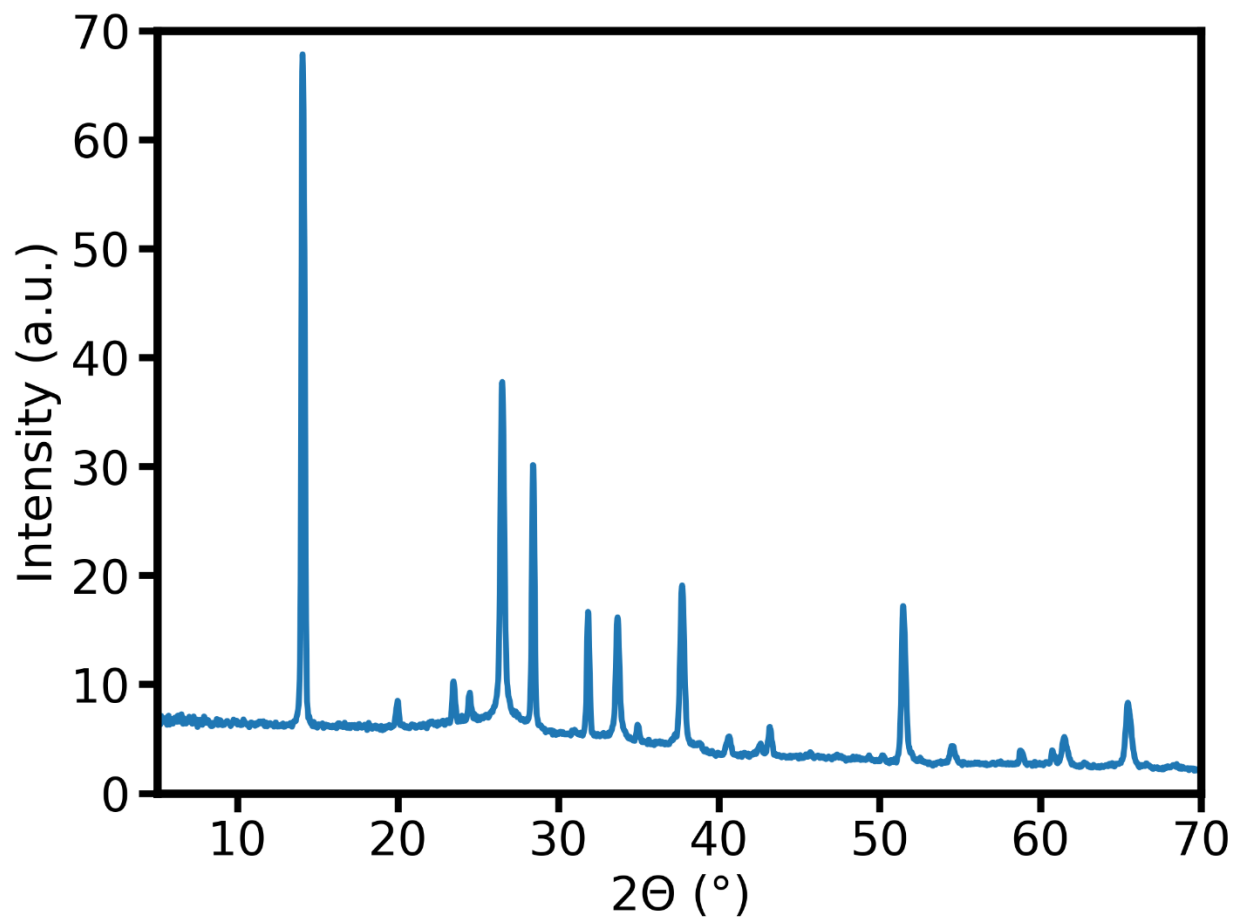
**Figure S1. XRD plot of a representative CH₃NH₃PbI₃ thin film on FTO substrate demonstrating the crystallinity of the film.**



**Figure S2. Inverse Pole Figure of CH₃NH₃PbI₃ thin films with individual back scatter diffraction patterns indexed to (a) tetragonal CH₃NH₃PbI₃ structure and (b) hexagonal PbI₂ for the same scan region.**
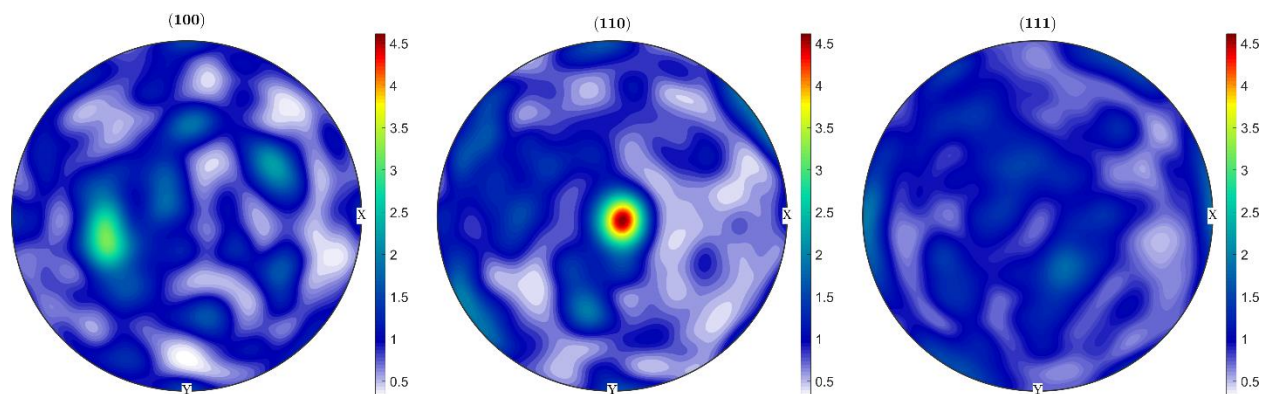
**Figure S3. Pole Density Figure. Projection of crystal orientations into the sample coordinate system. The color bars represent multiples of random distribution of orientations, meaning pole figure of a random standard sample would be '1x' at all points. Pole figure regions with intensities higher than '1x' demonstrate lattice planes that are preferentially aligned in those directions compared to a sample with random texture.**
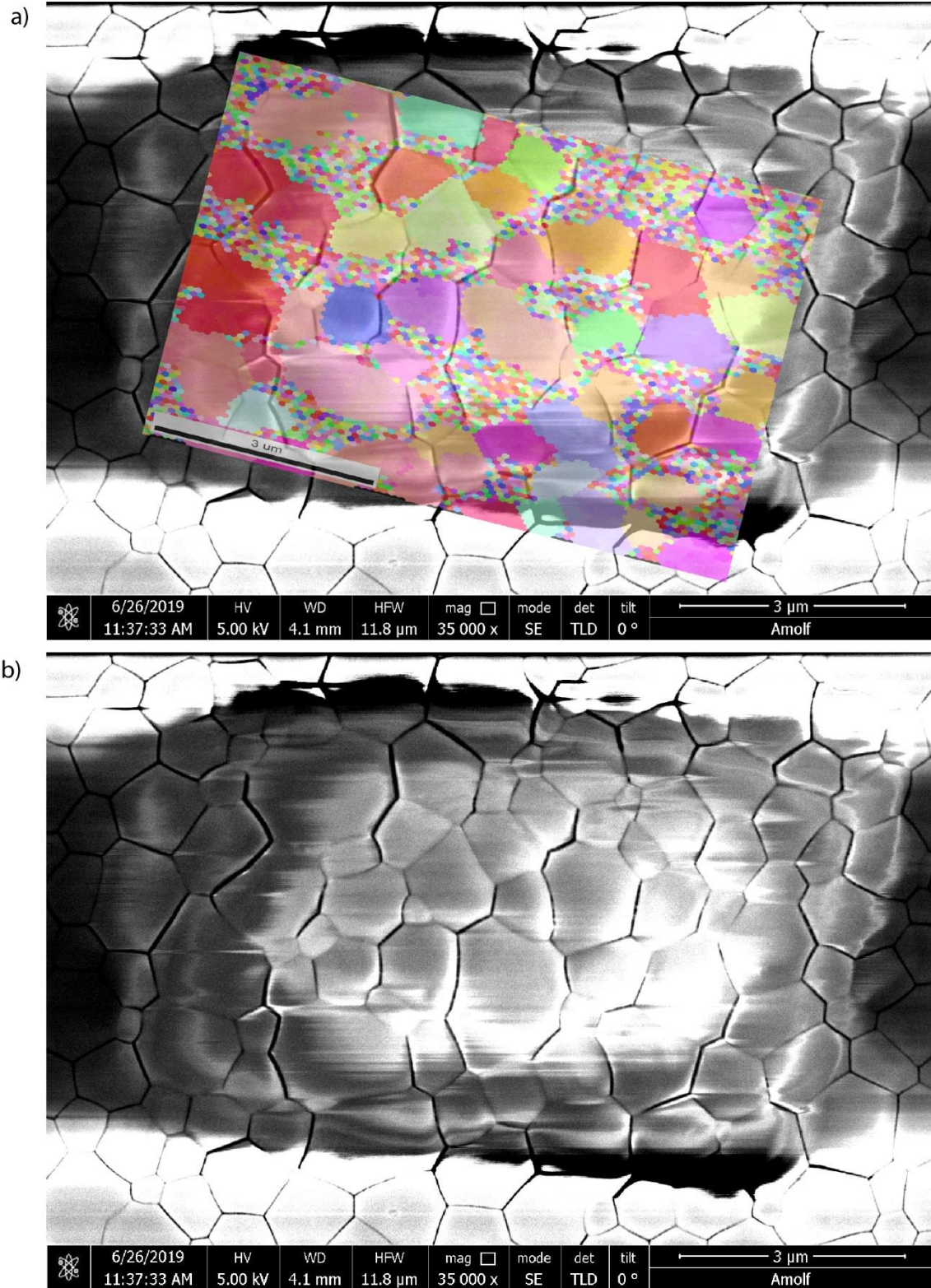
**Figure S4. Conventional SEM image at 0 degrees tilt and EBSD of the corresponding region. (a) Inverse Pole Figure (IPF) overlaid on top of the high-resolution SEM image. (b) High-resolution SEM image acquired after EBSD measurement. The white regions are due to charging effects.**
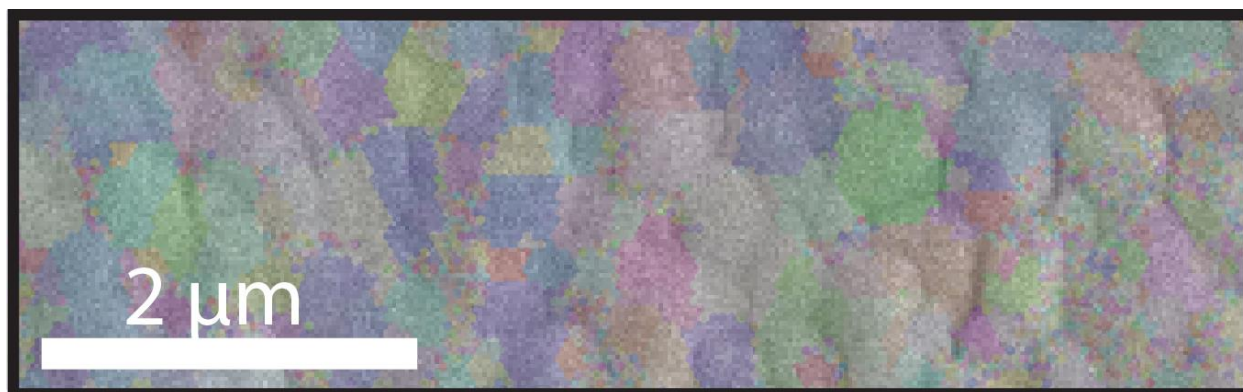
**Figure S5. Overlay of scanning electron microscope image and inverse pole figure (IPF) shown in Figure 1b and 1c in the main text.**
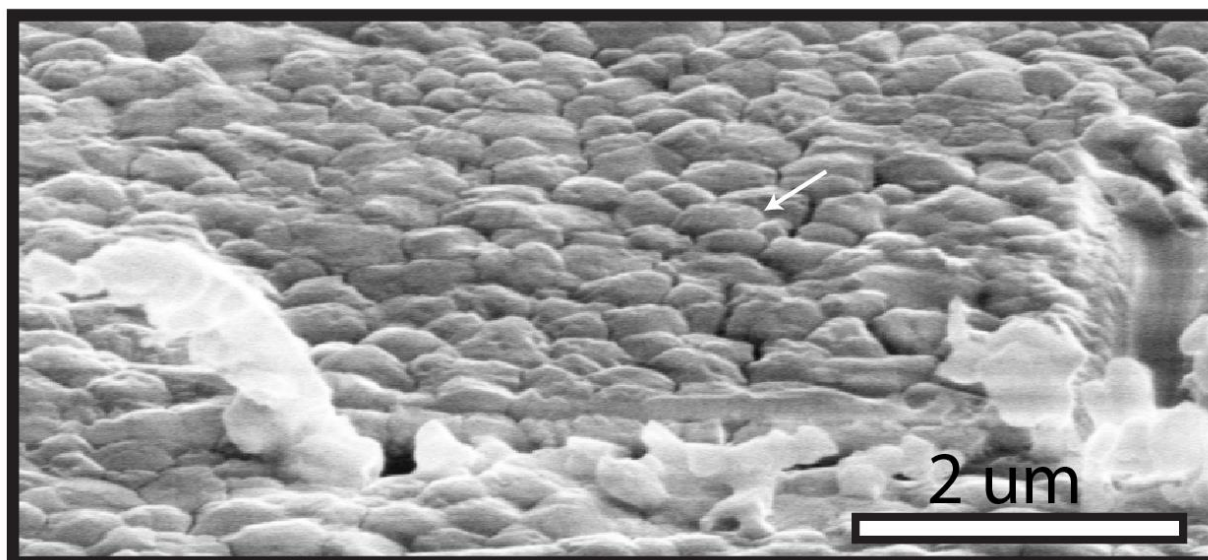


**Figure S6. Higher resolution SEM image (at 40° tilt) of the region in Figure 1b in the main text with scratch markers defining the ROI. The arrow shows the same region along the arrow in Figure 1b.**
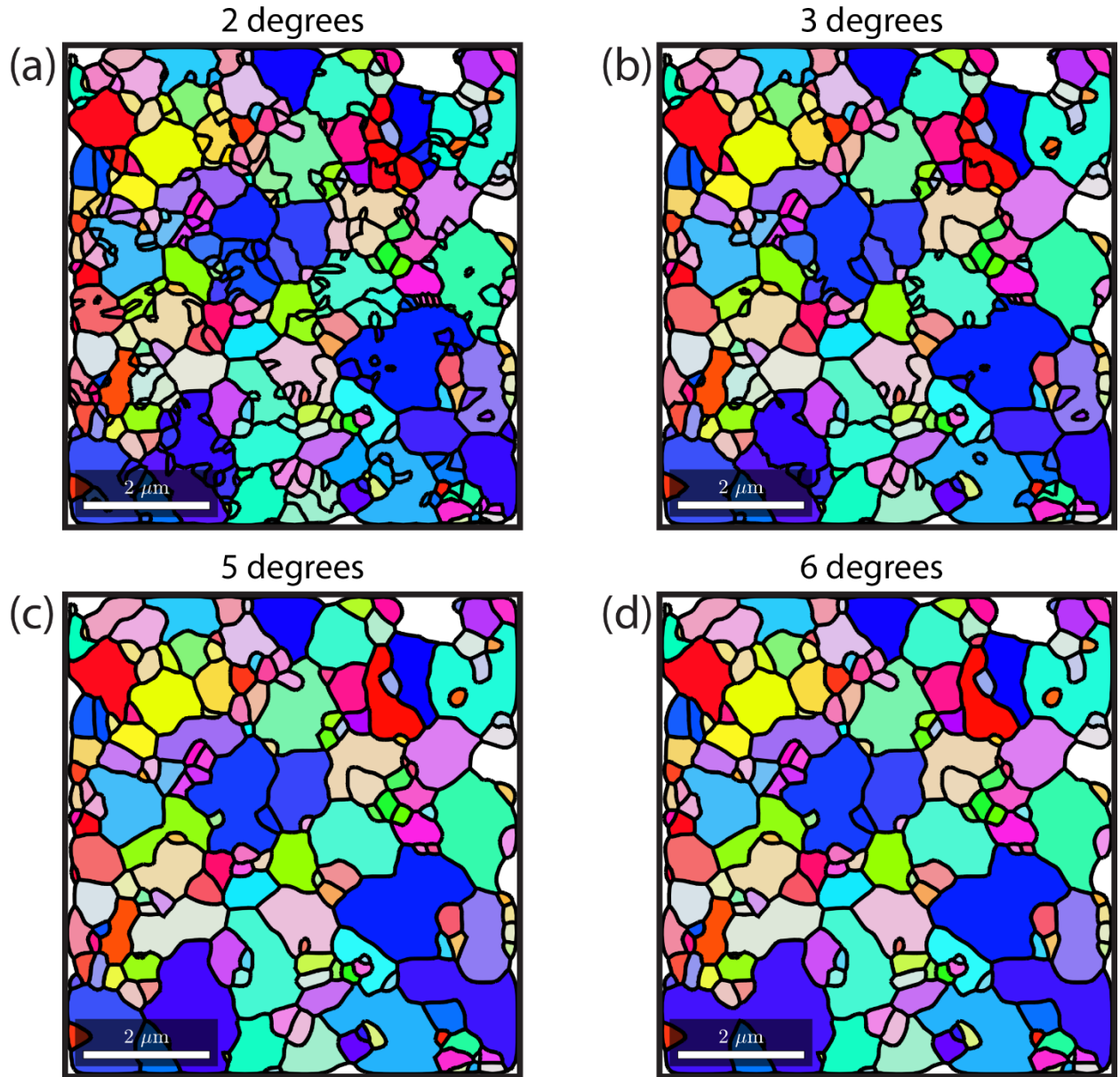
**Figure S7. Grain identification from IPF using different misorientation thresholds of (a) 2 degrees, (b) 3 degrees, (c) 5 degrees and (d) 6 degrees. Grains are plotted with their mean orientation. Refer Figure 2 in the main text for 4 degrees grain threshold and for color key.**
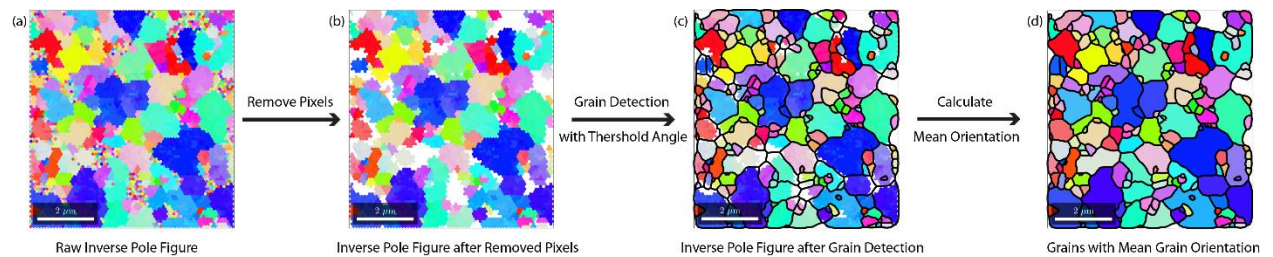
**Figure S8.** Grain identification process from raw inverse pole figure (IPF) to grains with mean orientation. (a) Raw IPF. (b) IPF after pixelated regions corresponding to one pixel grain are removed from the map. (c) Grain detection performed on resulting IPF from (b) with a threshold angle. The IPF is plotted with corresponding grains and grain boundaries that were identified. (d) Grain mean orientation is calculated and plotted with the corresponding grain boundaries.
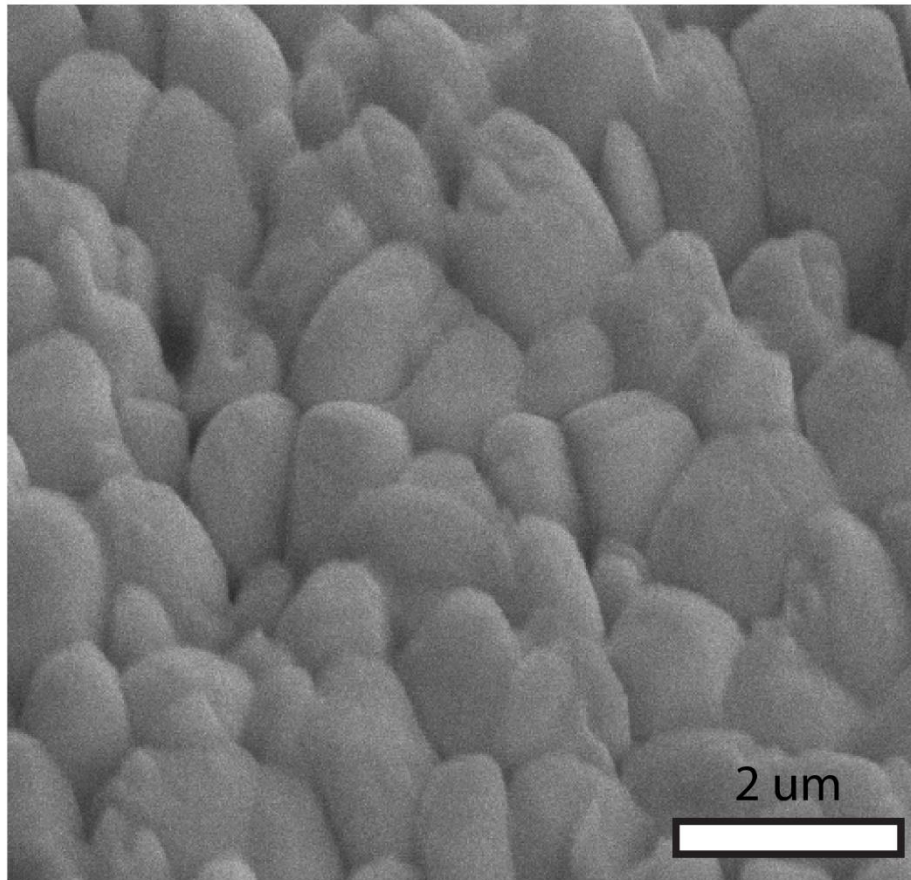


**Figure S9.** SEM image at 40° tilt of $CH_3NH_3PbI_3$ thin film for the region in Figure 2 in the main text.
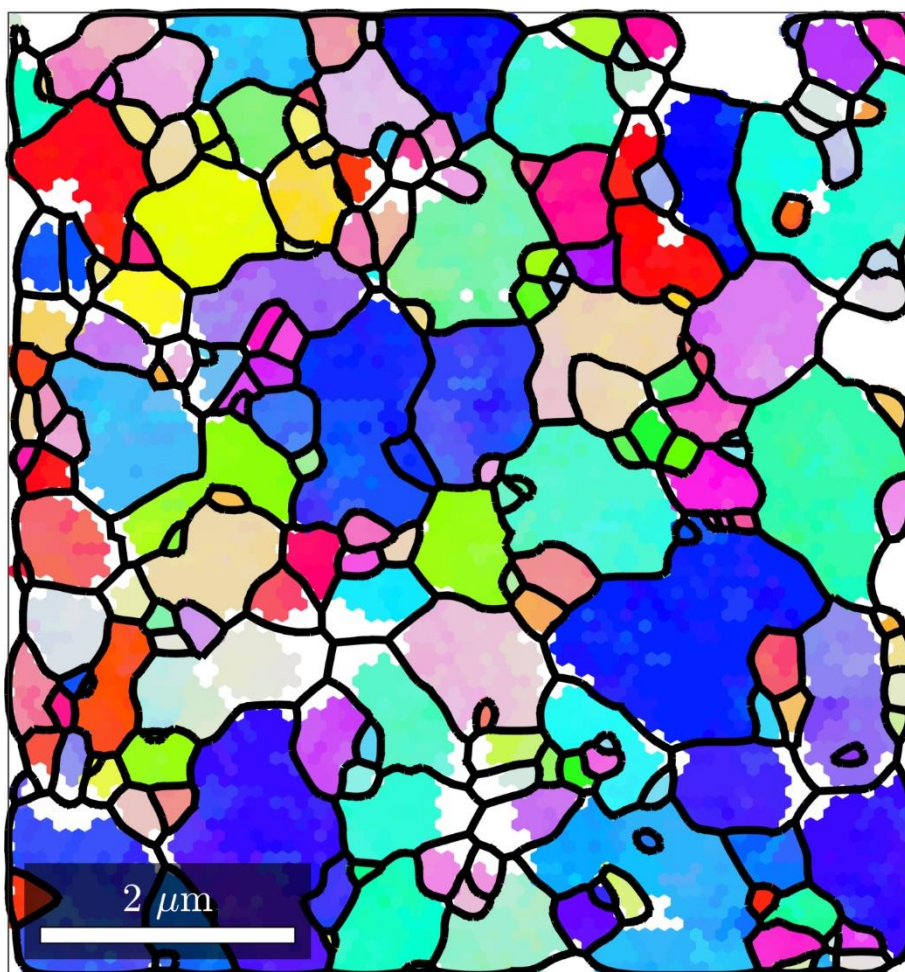
**Figure S10. Inverse Pole Figure (IPF) with grain boundaries after grain detection showing grain-to-grain orientation heterogeneity within the film. See Figure 2a and 2b in main text for IPF and plot of grains with mean orientation.**

Scan 1

Scan 2
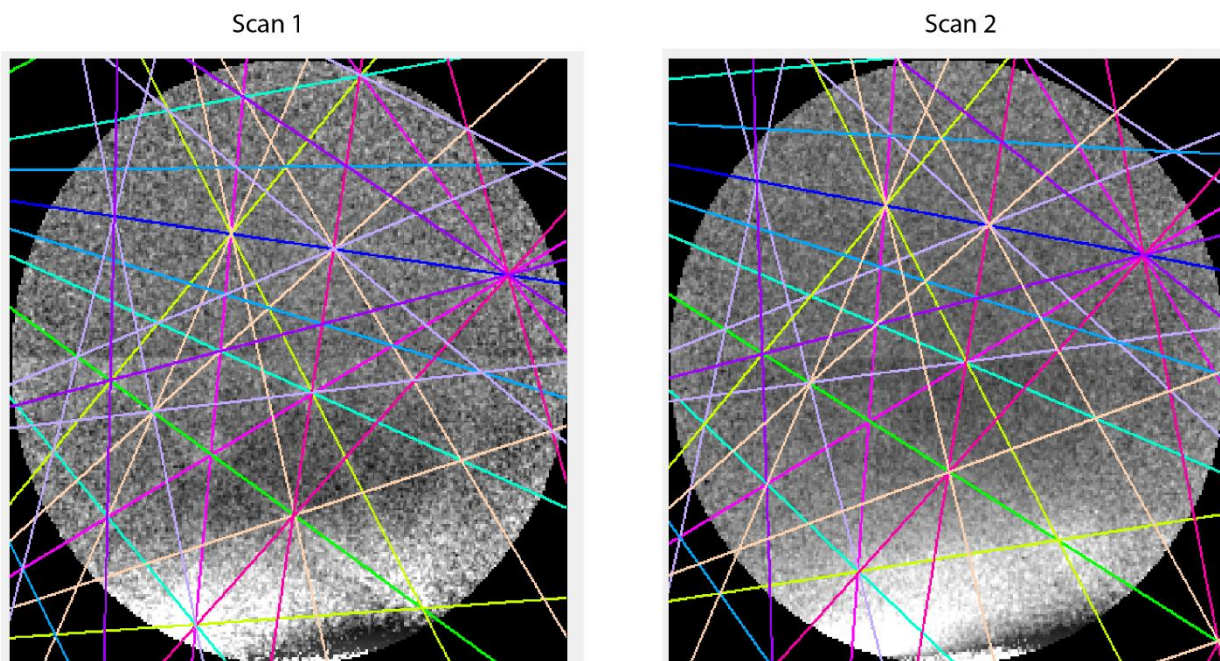


**Figure S11. Electron back scatter diffraction patterns of the same region from two consecutive scans showing that the pattern is present and indexed to the same crystallographic orientation of tetragonal CH₃NH₃PbI₃ after consecutive scans and, thus, demonstrating the minimal influence of electron beam induced damage on the overall results interpreted from the diffraction patterns.**
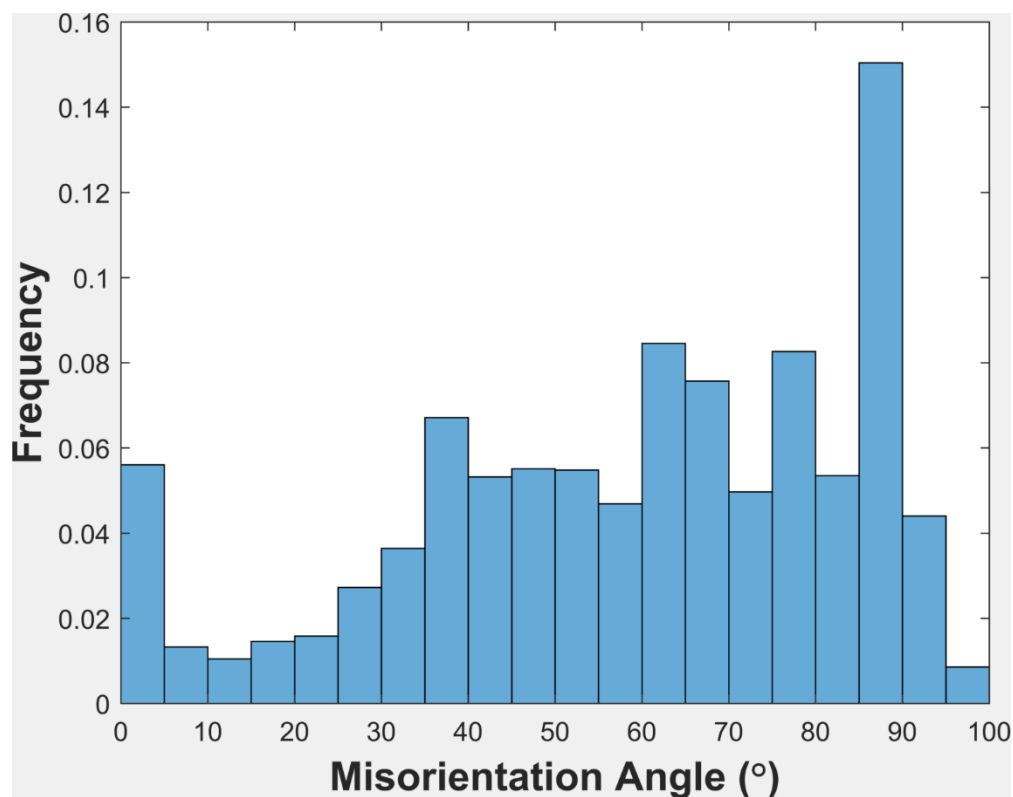
**Figure S12. Misorientation angle histogram showing the distribution of grain boundary misorientation angle in a representative CH₃NH₃PbI₃ thin film.**
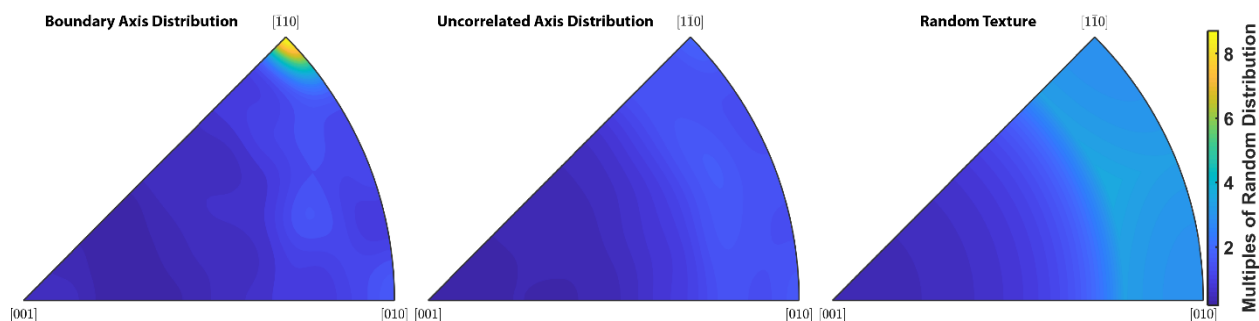
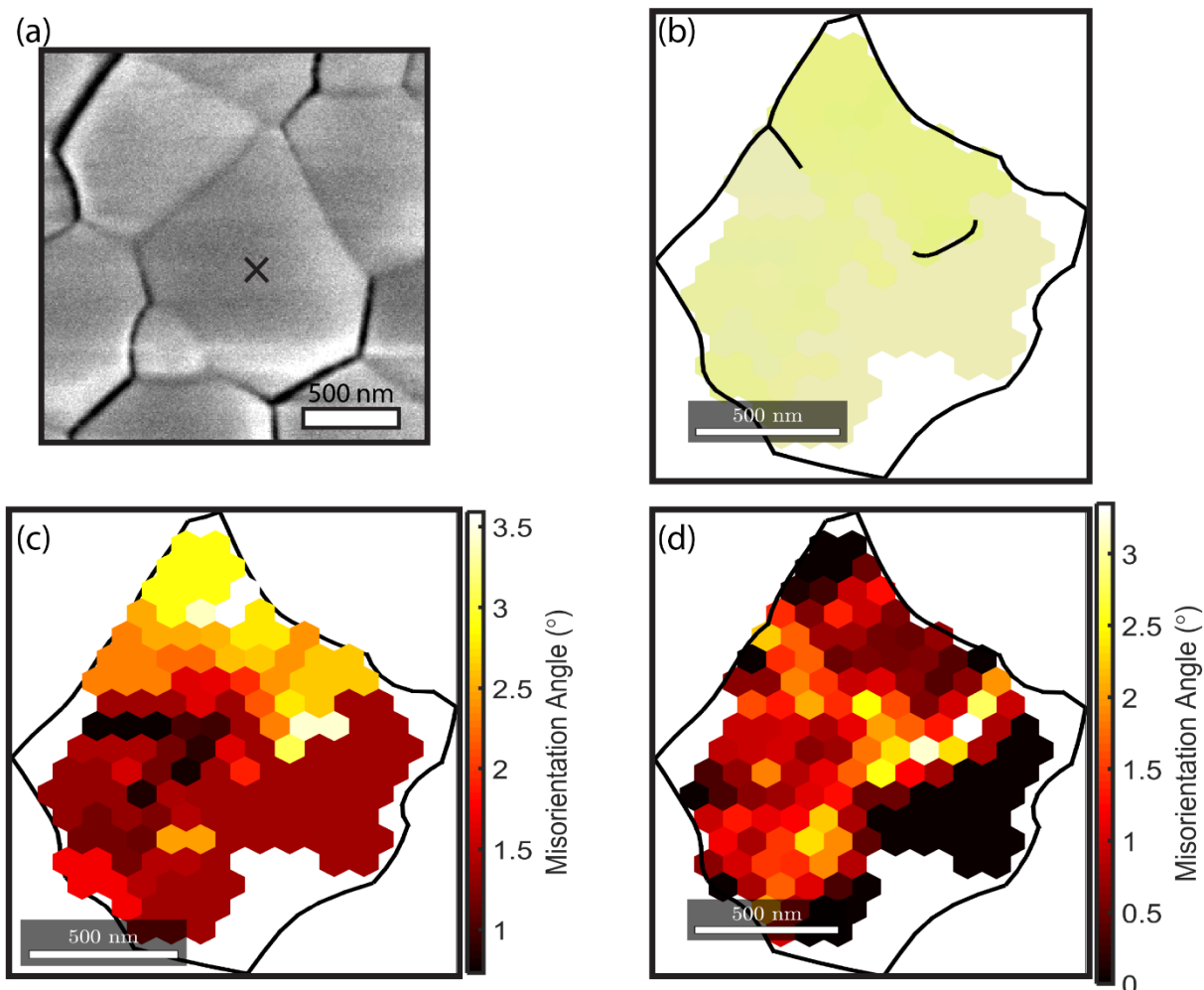

**Figure S13. Grain boundary misorientation axis distribution showing preferred orientation along [110] direction. Uncorrelated axis distribution is calculated using the uncorrelated misorientation (from points far from each other) and the underlying orientation distribution function. Misorientation axis distribution for random texture was calculated using random orientation distribution and crystal symmetry in the film.**
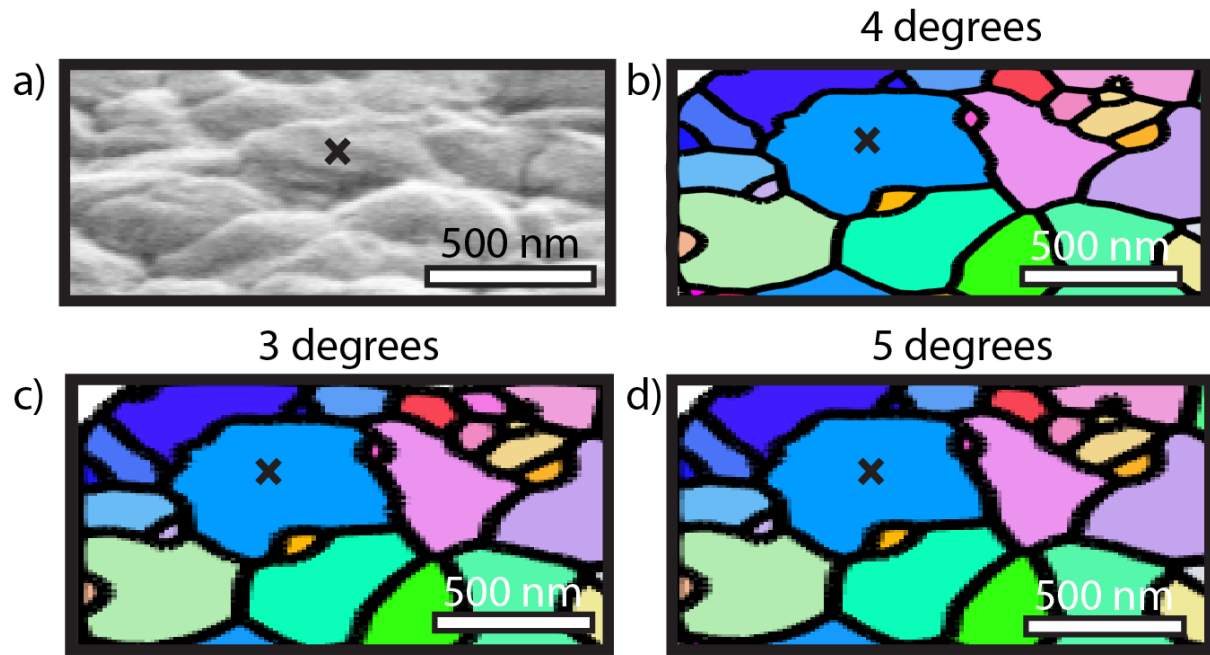
**Figure S14.** (a) SEM image at 40 degrees tilt and corresponding grains identified at different thresholds; (b) 4˚, (c) 3˚ and (d) 5˚; and plotted with their mean grain orientation. The grain marked with "X" represents the grain in Figure 3a in the main text.

**Figure S15. (a) High-resolution SEM image of a grain along with (b) Inverse Pole Figure (IPF) with sub-grain boundaries. (c) Kernel average misorientation (KAM) and (d) misorientation with respect to mean grain orientation of the same grain in (a) and (b). The grains were identified using a 4° threshold. The grains in (b), (c) and (d) correspond to the grain marked with "X" in the (a).**

IPF with Sub-Grain Boundaries

Kernel Average Misorientation

Misorientation w.r.t. Mean Grain Orientation
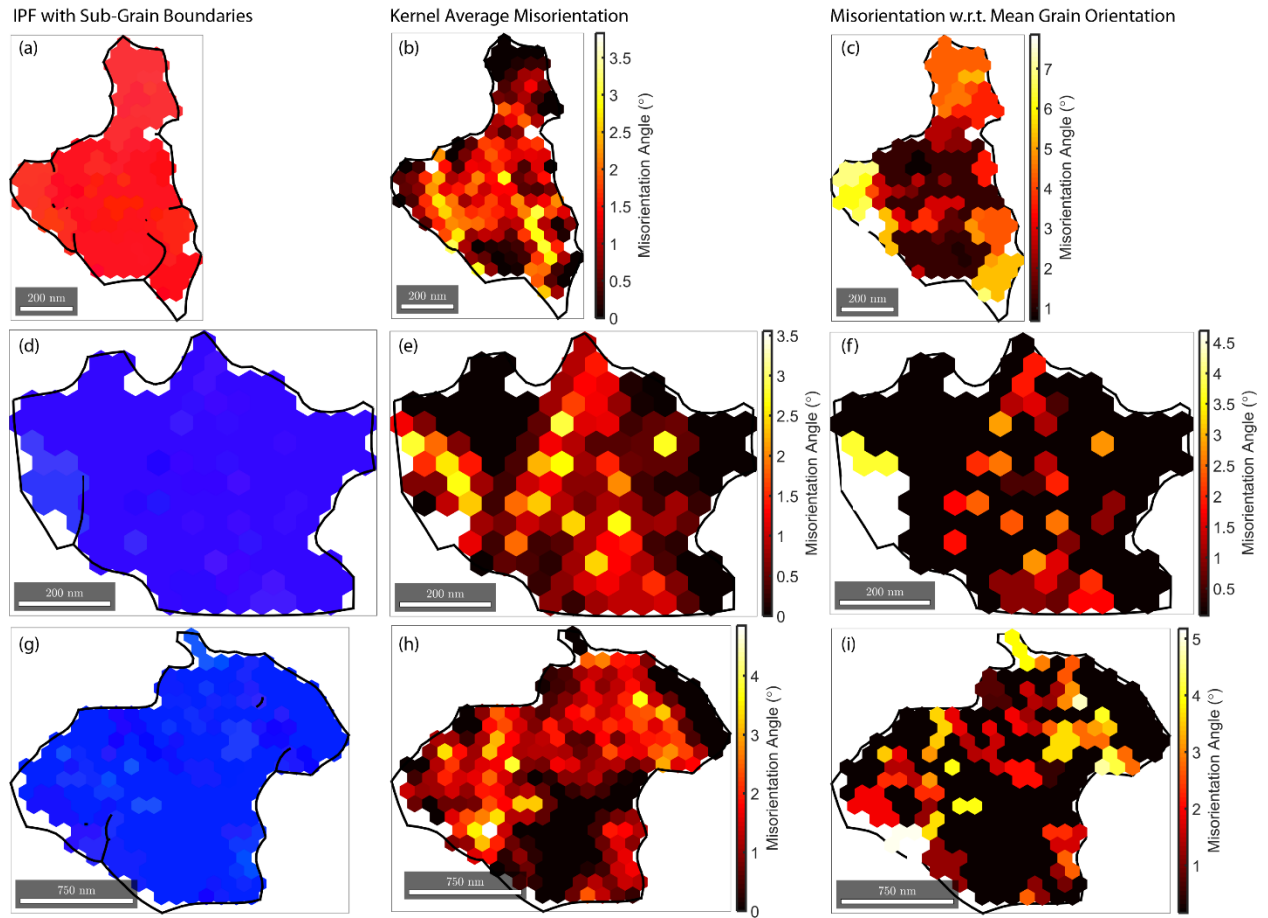


**Figure S16. Inverse Pole Figure (IPF) with sub-grain boundaries (a, d, g), kernel average misorientation (b, e, h) and misorientation with respect to mean grain orientation (c, f, i) for three different grains from different EBSD scans.**
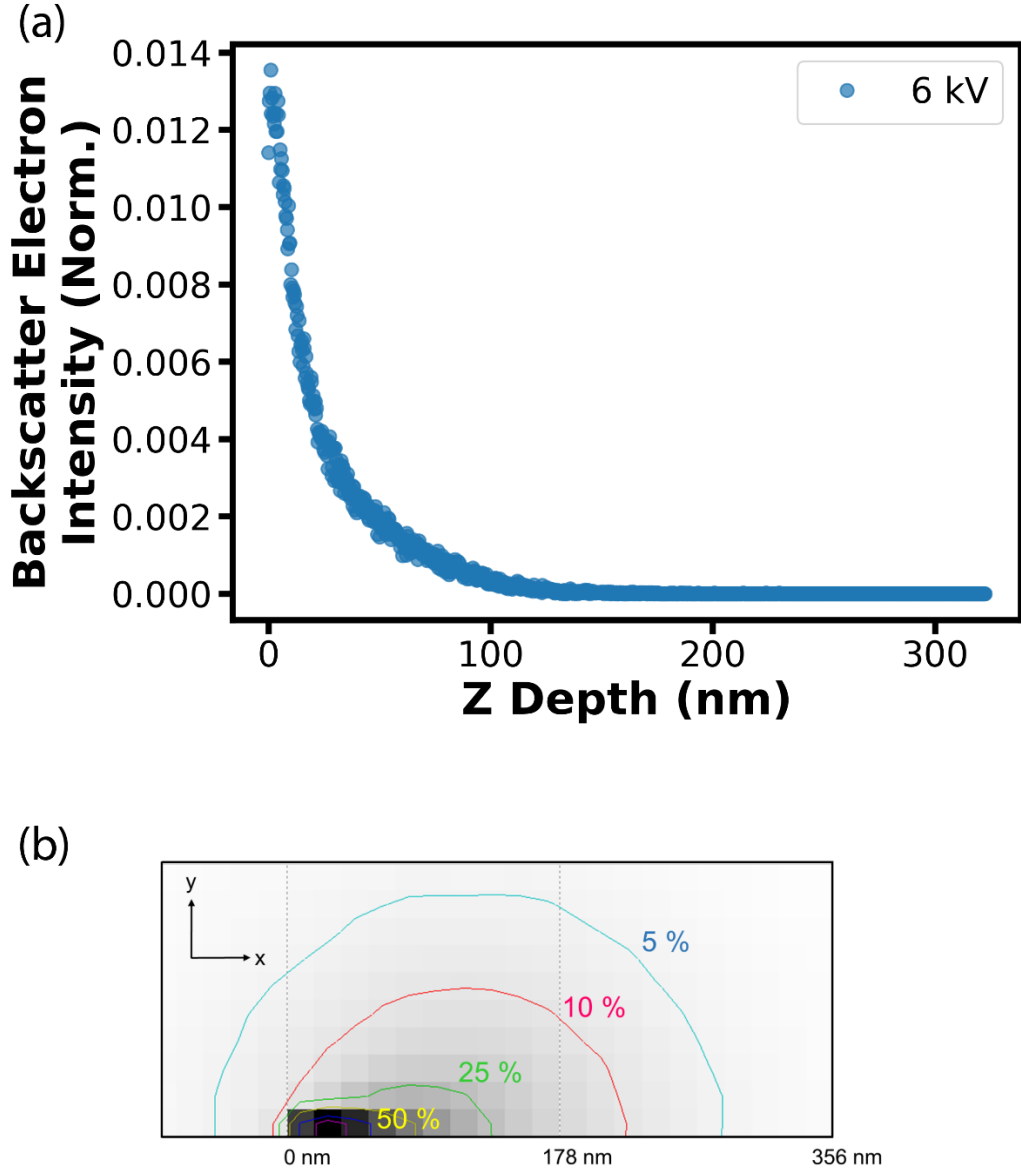
**Figure S17. Monte-Carlo simulation (using CASINO[12]) of electron interaction with CH₃NH₃PbI₃ showing backscatter electron intensity as a function of (a) z-depth in the film at 6kV accelerating voltage. The simulation was performed in traditional EBSD geometry (70° electron incidence with respect to the surface normal). This shows that the traditional EBSD geometry is more surface sensitive with a higher probability of backscattered electrons escaping from the perovskite surface. (b) X-Y plane profile of the back-scattered electron beam energy at 70° electron incidence with respect to the surface normal, showing ~37% backscattered electron energy distributed ~106 nm in the X-Y plane.**
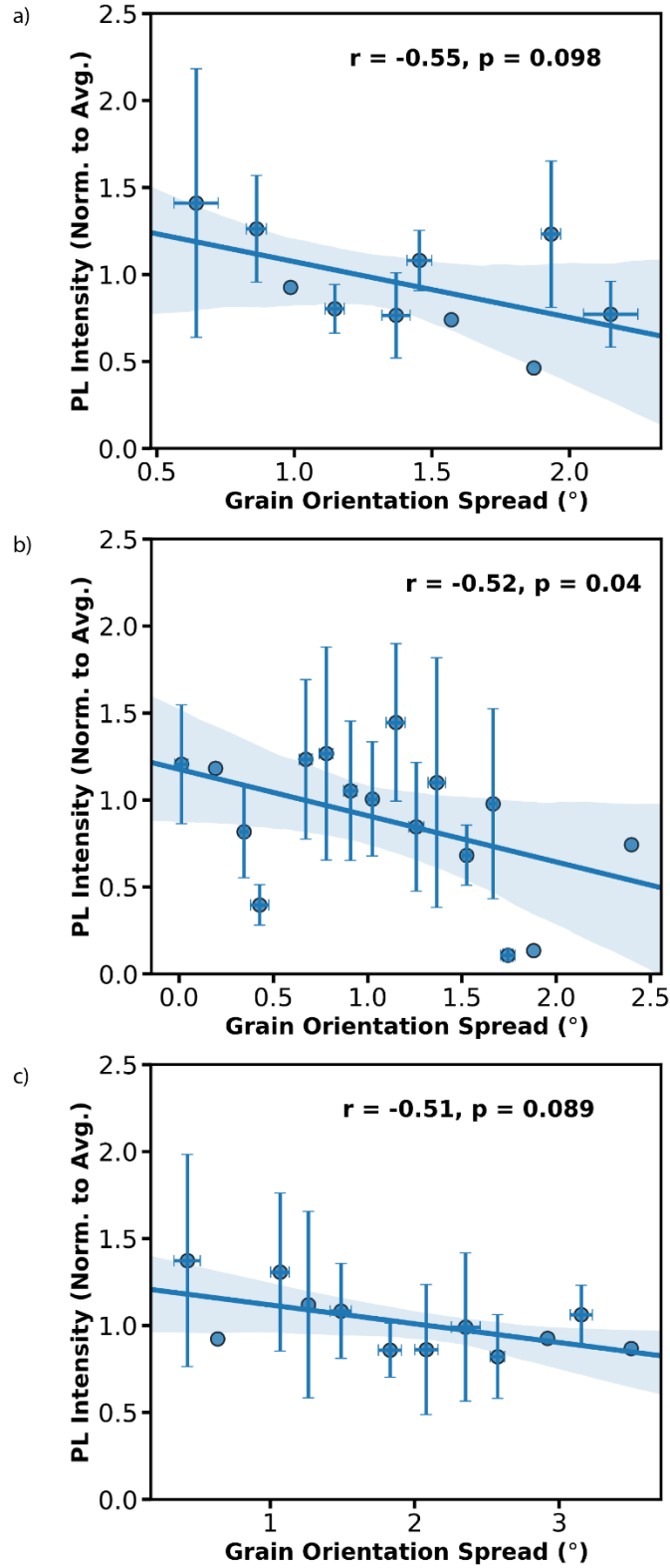
**Figure S18.** Correlation plot of PL intensity as a function of grain orientation spread (GOS) showing negative correlation for three different sample sets individually comprising of (a) 25 grains, (b) 80 grains and (c) 38 grains. The plots show anti-correlation with the line

**representing a linear regression fit to the data and shaded region representing 95% confidence interval. Error bars represent the standard deviation of the average PL intensity in a specific GOS interval.**
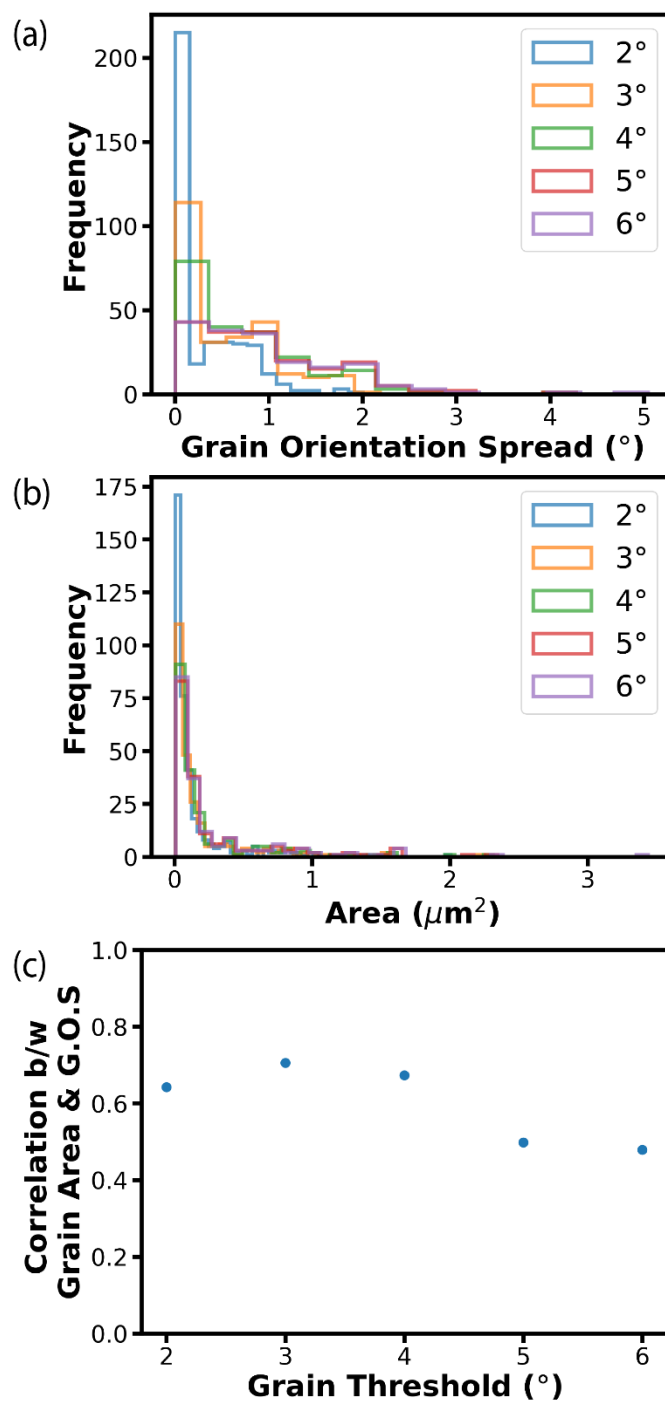
**Figure S19.** Histograms of (a) grain orientation spread (GOS) and (b) grain area for different grain threshold values. (c) Correlation between grain area and GOS at different threshold values showing strong positive correlation at all different grain threshold values.

**(a)**

**(b)**
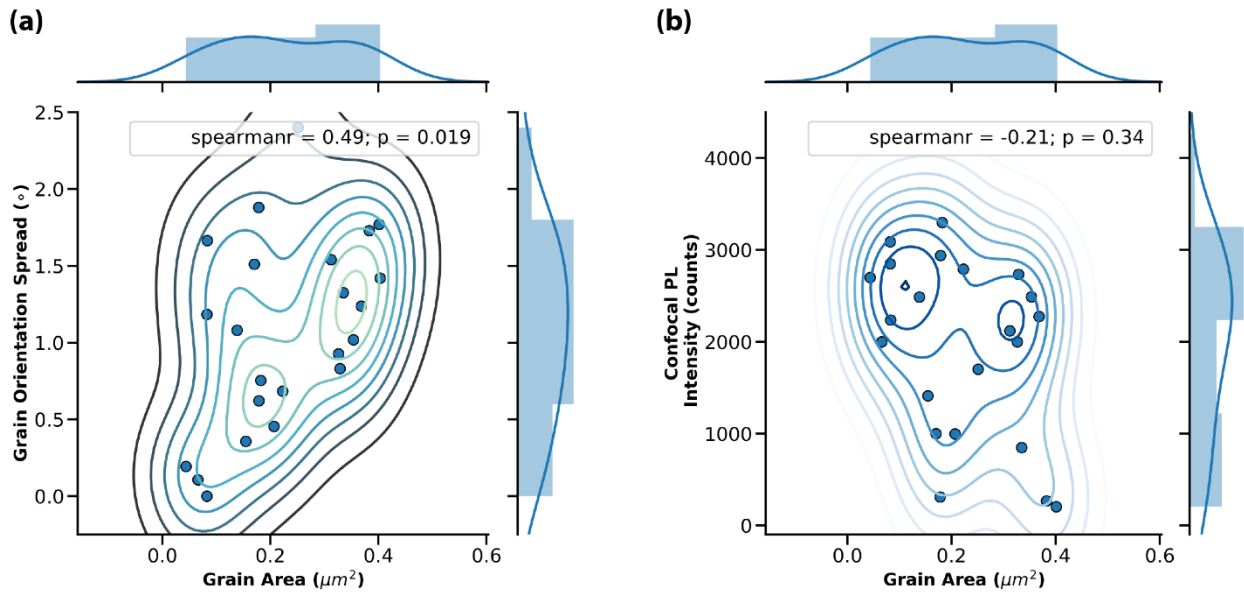


**Figure S20.** (a) Grain orientation spread within grains as a function of grain area showing positive correlation with high statistical significance (p = 0.019; p<0.05). (b) PL intensity measured at fluence corresponding to local trap density (see main text for more details) as a function of grain area showing very weak negative correlation with very low statistical significance (p = 0.34; p>0.05). The contours in (a) and (b) represent the kernel density estimate.

**References:**

[1]     Poglitsch A, Weber D. Dynamic disorder in methylammoniumtrihalogenoplumbates (II) observed by millimeter-wave spectroscopy. J. Chem. Phys. 1987;*87*:6373–8. doi:10.1063/1.453467.

[2]     Baikie T, Fang Y, Kadro JM, Schreyer M, Wei F, Mhaisalkar SG, et al. Synthesis and crystal chemistry of the hybrid perovskite (CH3NH3)PbI3 for solid-state sensitised solar cell applications. J. Mater. Chem. A 2013;*1*:5628. doi:10.1039/c3ta10518k.

[3]     Humphreys FJ, Huang Y, Brough I, Harris C. Electron backscatter diffraction of grain and subgrain structures - resolution considerations. J. Microsc. 1999;*195*:212–6.

[4]     Krieger Lassen NC. Source point calibration from an arbitrary electron backscattering pattern. J. Microsc. 1999;*195*:204–11. doi:10.1046/j.1365-2818.1999.00581.x.

[5]     Nowell MM, Wright SI. Orientation effects on indexing of electron backscatter diffraction patterns. Ultramicroscopy, vol. 103, 2005, p. 41–58. doi:10.1016/j.ultramic.2004.11.012.

[6]     Bachmann F, Hielscher R, Schaeben H. Texture Analysis with MTEX – Free and Open Source Software Toolbox. Solid State Phenom. 2010;*160*:63–8. doi:10.4028/www.scientific.net/SSP.160.63.

[7]     Nolze G, Hielscher R. Orientations - Perfectly colored. J. Appl. Crystallogr. 2016;*49*:1786–802. doi:10.1107/S1600576716012942.

[8]     Bachmann F, Hielscher R, Schaeben H. Grain detection from 2d and 3d EBSD data-Specification of the MTEX algorithm. Ultramicroscopy 2011;*111*:1720–33. doi:10.1016/j.ultramic.2011.08.002.

[9]     van der Walt S, Schönberger JL, Nunez-Iglesias J, Boulogne F, Warner JD, Yager N, et al. scikit-image: image processing in Python. PeerJ 2014;*2*:e453. doi:10.7717/peerj.453.

[10]    James G, Witten D, Hastie T, Tibshirani R. An Introduction to Statistical Learning with Applications in R. n.d.Springer; . doi:10.1007/978-1-4614-7138-7.

[11]    Jones, E., Oliphant, E., Peterson P et al. SciPy: Open Source Scientific Tools for Python 2001.

[12]    Demers H, Poirier-Demers N, Couture AR, Joly D, Guilmain M, de Jonge N, et al. Three-dimensional electron microscopy simulation with the CASINO Monte Carlo software. Scanning 2011;*33*:135–46. doi:10.1002/sca.20262.